ADVANCED FUNCTIONAL MATERIALS
www.afm-journal.de

Reevaluating the Activity of ZIF-8 Based FeNCs for Electrochemical Ammonia Production

*Caroline Schneider, S. Esmael Balaghi, Niklas Ortlieb, Patrick Elsaesser, Sima Heidari, Christopher S. Allen, and Anna Fischer**

The electrochemical reduction of N_2 in aqueous media and ambient conditions would present a great advancement in the defossilization of the fertilizer and energy sector, if the obstacles to this technology were not as significant as they are at present. Some recent reports have raised doubts about whether the electrochemical nitrogen reduction reaction (eNRR) is even possible in aqueous media. Herein, a type of metal-organic framework (MOF)-derived Fe and Zn single atom catalyst for the eNRR is revisited, which has been reported more than once in recent literature to be active for eNRR in aqueous media. Electrochemical measurements reported here show the inactivity of the investigated iron-based catalysts for the eNRR in neutral aqueous media when contaminations are excluded. In stark contrast, the reduction of NO_x contamination to ammonia is shown to be a possible reason for false positive results. The reduction of nitrate to ammonia (NO_3-RR) is itself an emerging field of research that investigates the conversion of nitrate from wastewater to ammonia. For the NO_3-RR, the MOF-derived catalysts show good activity and selectivity, which depends on the iron site density in the catalyst. An ammonia yield of 19.1 mg h^{-1} mg_{cat}^{-1} at −1.0 V versus RHE and a maximum faradaic efficiency (FE) of 100% at −0.9 V versus RHE is achieved.

1. Introduction

Ammonia is a compound of great importance because of its use in fertilizer production, explosives, and further chemical products, ever since the invention of the Haber-Bosch process enabled its production on an industrial scale.[1,2] In the past years, it has been further considered as a possible hydrogen carrier and clean energy carrier in the context of the defossilization of the global energy sector.[3] Hence, the worldwide ammonia demand is expected to increase heavily in the next few decades.[4,5] For the fertilizer sector alone, the market volume of ammonia is expected to increase to 300 Mt yr^{-1} in 2050 (90% increase compared to 2015) which is in the range of today's market volume of liquified petroleum gas.[5]

The Haber-Bosch process requires hydrogen, which is currently produced mostly from fossil fuels (99% of today's global hydrogen production), leading to CO_2 emissions and contributing to global warming.[6] In addition, high temperatures of 350–525 °C and high pressures of 10–30 MPa are necessary to react molecular nitrogen and hydrogen to ammonia.[1]

$$N_2\,(g) + 3H_{2(g)} \rightarrow 2\,NH_{3\,(g)}\,;\,\Delta_r H = -32\ \text{kJ mol}^{-1} \quad (1)$$

Today, hydrogen is mostly produced via steam reforming from natural gas (89.9% in 2023).[6] The Haber-Bosch process requires high amounts of fossil resources (1.8% of worldwide

C. Schneider, S. E. Balaghi, N. Ortlieb, P. Elsaesser, S. Heidari, A. Fischer
Albert-Ludwigs-Universität Freiburg, Institut für Anorganische und Analytische Chemie
Fakultät für Chemie und Pharmazie
Albertstraße 21, D-79104 Freiburg, Germany
E-mail: anna.fischer@ac.uni-freiburg.de

C. Schneider, S. E. Balaghi, N. Ortlieb, S. Heidari, A. Fischer
FMF – Freiburg Material Research Center
Stefan-Meier-Straße 21, D-79104 Freiburg, Germany

S. E. Balaghi, P. Elsaesser, S. Heidari, A. Fischer
FIT – Freiburg Center for Interactive Materials and Bioinspired Technologies
Georges-Köhler-Allee 105, D-79110 Freiburg, Germany

S. Heidari, A. Fischer
Cluster of Excellence Living, adaptive and energy-autonomous Materials Systems (livMatS), FIT–Freiburg
Center for Interactive Materials and Bioinspired Technologies
Georges-Köhler-Allee 105, D-79110 Freiburg, Germany

C. S. Allen
Physical Science Imaging Centre
Diamond Light Source Ltd.
Oxford OX11 0DE, UK

C. S. Allen
Department of Materials
University of Oxford
Parks Road, Oxford OX1 3PH, UK

The ORCID identification number(s) for the author(s) of this article can be found under https://doi.org/10.1002/adfm.202513254

DOI: 10.1002/adfm.202513254

consumption) and causes significant CO_2 emissions (>1% of global CO_2 emissions).[7] With regard to global warming and global efforts to reduce greenhouse gas emissions, a less CO_2 intense process for ammonia production is highly desirable.

In the 1960s, the idea of the electrochemical N_2 reduction reaction (eNRR) to ammonia in aqueous media and ambient conditions was born.[8] In an electrochemical cell, N_2 and protons are reduced to ammonia at the cathode and water is split into protons and O_2 on the anode. Powered with renewable electricity, the process would cause low CO_2 emissions and could be implemented at various scales wherever electricity is available. However, there were rather few researchers who pursued this idea until considerable attention was drawn to eNRR from 2015 onward.[9]

To be economically viable, the performance of the eNRR systems would need to be comparable to the Haber-Bosch process in terms of energy efficiency. The US Department of Energy has set the target of 60% energy efficiency for electrochemical nitrogen to ammonia electrolysis cells.[5,10] To reach these targets, an efficient and selective catalyst must be developed, and the process conditions must be optimized for optimum energy efficiency and yield rates.

The electrochemical reduction of nitrogen in aqueous electrolytes requires N_2 dissolved in the electrolyte as well as eight protons and six electrons to yield two molecules of ammonia. The reaction takes place as follows in acidic and neutral media:[11]

$$N_{2\,(g)} + 8\,H^+ + 6\,e^- \rightarrow 2\,NH_4{}^+{}_{(aq.)} \qquad E^\circ = 0.274\ V_{RHE} \tag{2}$$

The oxidation of water follows:

$$2H_2O_{(l)} \rightarrow O_{2\,(g)} + 4e^- + 4\,H^+ \qquad E^\circ = 1.229\ V_{RHE} \tag{3}$$

So that the overall reaction in acidic and neutral is

$$6H_2O_{(l)} + 2N_{2(aq.)} + 4H^+ \rightarrow 3O_{2(g)} + 4NH_4{}^+{}_{(aq.)}$$
$$\Delta E^\circ = 0.995 V_{RHE} \tag{4}$$

The eNRR is altogether challenging to realize, especially in aqueous media. The solubility of N_2 in water (19 mg $kg_{water}{}^{-1}$ at 1 atm)[12] is very low in comparison with O_2 and CO_2 (44.33 and 1690 mg $kg_{water}{}^{-1}$, respectively), which limits the availability of the reactant.[13] Also, the adsorption of N_2 on the electrode and its reduction competes with the adsorption of protons and their reduction to H_2.[13] During the reaction, the binding energy of the triple N≡N bond of 941 kJ mol^{-1} must be overcome so that ammonia can be formed.[10] Selectivity also poses problems, as the hydrogen evolution (HER) reaction takes place at similar potentials and is often kinetically favored.

$$2H^+ + 2e^- \rightarrow H_{2\,(g)} \qquad E^\circ = 0 V_{RHE} \tag{5}$$

Many efforts have been dedicated to the investigation of promising catalysts, possible mechanisms, and suitable reaction conditions for the eNRR with the aim of building a selective and high-yield system. Numerous catalytic systems have been proposed, but still the question remains if it is actually feasible to reduce N_2 to NH_3 in heterogeneous electrocatalysis. Various publications state ammonia yields of picomoles to nanomoles ammonia per second per square centimeter, which raises the question of whether these yields are significant and reproducible and whether they evolve from actual electrochemical reduction of N_2 in aqueous media.

Shortly after the eNRR gained considerable attention starting in 2015,[14] it was realized that reducible nitrogen species in the electrochemical cell pose a problem.[15] Kim et al. reported that their ammonia yields were at least partly resulting from the reduction of ethylenediamine contained in the electrolyte.[16] The aspect of falsified ammonia yield rates through the reduction of other N-species than N_2 was understood, but its importance was still underestimated. Also, the presence of ammonia in air and human breath was realized and taken into account as an extraneous source of ammonia.[15] In 2019, the group of A. N. Simonov reported a "critical assessment" of transition metal nitrides refuting the idea that the Mars-van-Krevelen mechanism could contribute to eNRR in aqueous electrolyte.[17] The ammonia yield was attributed to the decomposition of the nitride material, and it was questioned for the first time if N_2 can be reduced in aqueous media at all.

Finally, nitrates, nitrites, and gaseous NO_x species were identified as N-species that yield ammonia upon reduction and hence lead to overestimated ammonia yield rates for eNRR. This was brought to the attention of the community by Chorkkendorff and coworkers.[18] Consequently, catalysts that had been claimed active for the eNRR were revisited and found active for the reduction of NO_x species, but inactive for eNRR.[19] The questions ensued whether further catalysts exhibit NO_x reduction activity and no eNRR activity, and whether eNRR in aqueous media is possible at all. At this point, the reliability of previous reports on eNRR was challenged. Criteria for the reassessment of previous reports were established, and many reports were deemed unreliable.[20]

Both Chorkkendorff and MacFarlane et al. emphasized the importance of a rigorous eNRR performance protocol for conducting experiments, as well as importance of reporting all relevant experimental parameters to enable others to assess the reliability of future results.[18,20] Further reports complemented these criteria with aspects related to ammonia quantification, the proton-conducting membrane, and additional factors.[21–24]

The criteria for reliable eNRR experiments are:

1) Is the ammonia quantification method reliable?[25,26] If yes, ammonia is detected at concentrations in the μM range reproducibly.
2) Is the amount of ammonia significant?[20,24] If yes, the amount of ammonia produced in the electrochemical reaction is significantly larger than the background levels of ammonia.
3) If ammonia is found, where does it originate from? Is ammonia also formed when the same experiment is run under an argon atmosphere? Do the electrodes or the membrane of the H-cell release ammonia?[15] If yes, the ammonia does probably not originate from the reduction of N_2.
4) Does the gas feed contain ammonia? Does it contain nitrous oxides? Is a gas cleaning/scrubbing system implemented before the experiment?[20] Does the electrolyte contain nitrates or nitrites? Do the electrodes or membrane release nitrates or nitrites? All possible sources of contamination must be excluded.

5) If isotope labelling experiments are done, are the yields and efficiencies the same for ^{14}N and for ^{15}N? Are the isotope labeling experiments following all requirements for reliability?[18,20] The $^{15}N_2$ gas must also be free from contaminants.

With these criteria established, several reports have been published that revisit different eNRR catalysts and find them inactive.[27–29]

One class of materials that has been of interest as catalysts for the eNRR are iron single atom sites. In the first place, the natural enzyme nitrogenase inspired these catalysts as the active center consists of a complex iron-sulfur cofactor.[30] Iron-dinitrogen complexes were also employed in homogeneous catalysis of the reduction of N_2 to ammonia.[31] Also, iron single atoms have been investigated for the eNRR in theoretical calculations that came to predict eNRR catalytic activity for these materials.[32] Following these reasons, different kinds of iron single atoms supported on N-doped carbons (FeNCs) have been synthesized and investigated for the eNRR.[33–38]

Among these single atom catalysts (SACs), several were synthesized in two steps involving the synthesis of an iron doped metal organic framework (MOF) – often a zinc-imidazole framework (ZIF-8) – with subsequent pyrolysis. This synthesis strategy is comparably facile and has been widely employed for the synthesis of FeNC materials for the catalysis of the oxygen reduction reaction (ORR).[39,40] In the field of ORR, the iron centers were researched extensively[41,42] and this knowledge is helpful when using FeNC materials for the eNRR.

For example, a ZIF-8-based FeNC has been reported active for eNRR by Lü et al. with a reported ammonia yield rate of 62.9 µg h^{-1} mg_{cat}^{-1} and a faradaic efficiency (FE) of 18.6%.[34] The above-mentioned criteria for reliable eNRR activity determination are however not fully met in the study, so that the reported ammonia yield rates cannot be verified independently. For example, NO_x species have not been quantified in the ammonia production measurements. Hence, the reported publication leaves open the possibility that the N_2 gas feed was contaminated by NO_x species that were reduced to ammonia during electrochemical investigations, potentially leading to an overestimation of the ammonia yields at best. At worst, a material may have been reported to be eNRR-active when it is not.

A similar catalyst – a FeZnNC dual atom site catalyst – has been reported by Zhang et al.[37] This catalyst consists of FeN_x- and ZnN_x single atom sites on a porous carbon support and was synthesized via complexation of the metal ions by chitosan and subsequent pyrolysis. Its ammonia yield from eNRR is reported to be 30.5 µg h^{-1} mg_{cat}^{-1} at −0.3 V versus RHE with a FE of 26.5%. Also, in this case, NO_x contaminations were not quantified, which raises again the question of the reliability of these findings.

Also, a MOF-based N-doped carbon material has been synthesized and claimed to be active for the eNRR.[43] Afterward, however, the inactivity for eNRR has been demonstrated experimentally and theoretically.[20,44] In this overall context, the class of ZIF-8 derived FeNC materials as catalysts for the eNRR is worth revisiting.

The electrochemical reduction of nitrate, nitrite or gaseous NO_x species is not only an undesired contaminant reaction in the field of eNRR but also a research field of its own.[45–49] Ammonium and nitrate salts are used for fertilizer production and cause severe pollution when they are washed into groundwater and surface water bodies. If contained in high concentrations in drinking water, nitrate can lead to illness in infants (Blue Baby Syndrome) and pose a threat to human health.[50] As sweet water is a limited resource, responsible fertilizer use and water consumption are required, as well as technologies to remove pollutants from groundwater. In this context, electrochemical nitrate reduction (NO_3-RR) is considered a green technology to remove nitrate from drinking water. Nitrate can be reduced electrochemically to dinitrogen or ammonia. The reduction of nitrate to N_2 would simply remove the nitrate from the water. However, the reduction of nitrate to ammonia would create a value-added product that is highly desirable.[51,52]

The electrochemical reduction of nitrate to ammonia follows:

$$NO_3^-{}_{(g)} + 10\ H^+ + 8e^- \rightarrow NH_4^+{}_{(aq.)} + 3H_2O_{(l)}$$
$$E^\circ = 0.88V_{RHE} \quad (6)$$

Side products from nitrate reduction experiments are usually nitrite, N_2 and H_2. The challenge in the development of NO_3-RR catalysts is to achieve high ammonia selectivity and high ammonia production rates. Among the N-doped graphene supported single atom sites, iron is reported to be the metal closest to the top of the volcano plot for nitrate to ammonia reduction and simultaneously having the highest selectivity for ammonia.[53] For iron metal surfaces, N_2 is predicted to be the main product of nitrate reduction.[54] Consequently, it is of great importance to produce iron single atom sites selectively in order to obtain an active and selective catalyst. In further detail, graphene supported Fe-N_4 sites with pyrrolic and pyridinic N groups have been investigated in DFT calculations. The iron single sites coordinated by pyrrolic N only were predicted to show higher NO_3-RR performance than the Fe-N_4 coordinated by pyridinic groups.[55,56] In order to produce the pyrrolic Fe-N_4 sites, a synthesis introducing iron-pyrrole complexes as precursors is very suitable. In that context ZIF-8-based synthesis routes are of interest if, for example, iron-imidazole or iron-porphyrin complexes are used as iron precursors.

In experimental reports, mesoporous FeNC materials have been reported to be active by Li et al. and Zhao et al.[57,58] Both FeNC catalysts have been synthesized via the pyrolysis of a templated polypyrrole. The FeNC by Wu et al. has an Fe content of 1.51 wt.% and it exhibits an activity of 5.2 mg h^{-1} mg_{cat}^{-1} in neutral 0.5 M KNO_3 at −0.7 V versus RHE.[58] The catalyst of the Li group contains 2.38 wt.% Fe and exhibits a yield rate of 2.75 mg h^{-1} cm^{-2} at −0.7 V versus RHE in alkaline 0.1 M KNO_3 solution.[57] The faradaic efficiencies are 75% and 100% respectively.[59] To the best of our knowledge, a ZIF-8 derived FeNC catalyst has not been reported for the electrochemical nitrate reduction. In addition, Zn single atom sites supported on N-doped carbon were investigated for the NO_3-RR, and good ammonia yields and FE have been reported.[49] In 5 mM $NaNO_3$ in 0.1 M Na_2SO_4, the ZnNC produced ammonia yields of 39 mg h^{-1} mg_{cat}^{-1} at −1.0 V versus RHE and 95% FE at

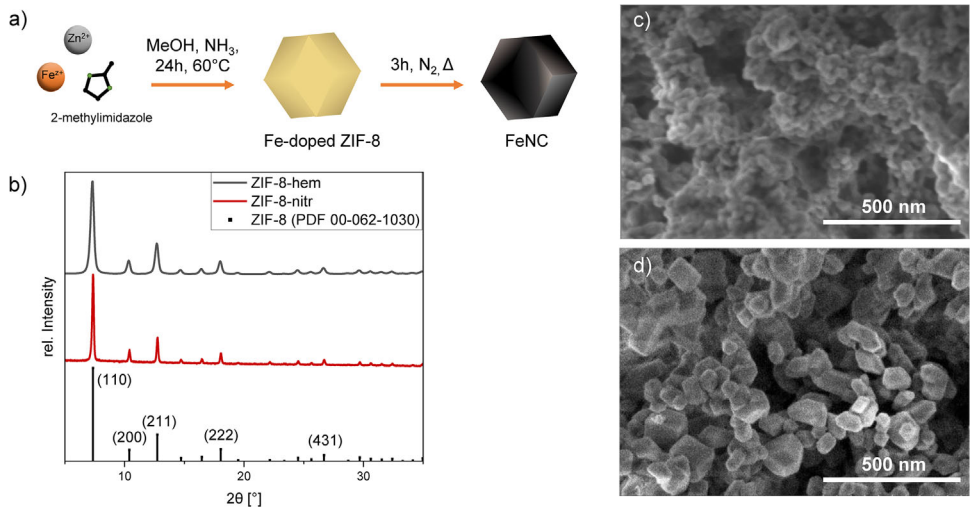

Figure 1. An Fe-doped ZIF-8 is precipitated from solution and pyrolyzed to obtain an Fe- and N-doped carbon material (FeNC) as shown in scheme (a). The X-ray diffraction pattern of the pristine and F-edoped ZIF-8 materials are shown in (b), scanning electron micrographs (SEM) of ZIF-8-hem in (c) and of ZIF-8-nitr in (d). The SEM images were recorded at 1 kV acceleration voltage, 4 mm working distance, and 100 k fold magnification using secondary electron plus backscattered electron (SE +BSE(U)) detector.

−0.9 V versus RHE. It must be noted that the ZnNC was measured not only at a lower nitrate concentration, but also with a much lower loading on the working electrode than the FeNC catalysts. Consequently, direct comparison is impossible. However, the ZnNC shows higher FE for ammonia at higher potentials than the FeNC. Combining the lower onset potential of the FeNC catalysts and the higher efficiency of the ZnNC catalysts could be beneficial if combined.

To summarize, the idea of electrosynthesizing ammonia from N_2 in aqueous media and under ambient conditions could be highly beneficial if it proves feasible. In that context, ZIF-8 based FeNC materials are an attractive class of catalysts and have been reported to be active for the eNRR in neutral aqueous media. However, due to numerous doubts voiced in recent years, the ZIF-8 based FeNCs catalysts are revisited in this work. Fe-doped ZIF-8 was synthesized and identified as such by powder X-ray diffractometry. After calcination, the final FeNCs were carefully analyzed using numerous complementary characterization methods, revealing the single site nature of the materials. The FeNC materials were tested for eNRR performance following the requirements for reliable eNRR reports. However, the amounts of ammonia detected were close to zero and could be attributed to the reduction of N-species of the catalyst.

In order to avoid any false results from contamination from the catalyst, the order of blank before performance measurement must be strictly respected. The presence of NO_x species in N_2 feed gas and their reduction to ammonia is generally considered a possible explanation for false positive eNRR results. For this explanation to be viable, the FeNC catalysts need to be active for the reduction of NO_x species to ammonia. It could be shown that this is the case.

As the ZIF-8 based FeNC was predicted to be active for the NO_3-RR and we demonstrated their activity for the reduction of different NO_x species at low concentration, it was obvious to test the nitrate reduction activity at high nitrate concentration, also to compare it to other FeNC catalysts reported. Our FeNCs achieved an ammonia production rate of 19.1 mg h^{-1} mg_{cat}^{-1} ammonia production at −1.0 V versus RHE and a maximum FE of 100% at −0.9 V versus RHE.

2. Synthesis and Characterization

The FeNC materials were synthesized in two steps (**Figure 1a**). First, the precursors, Fe-doped ZIF-8 materials were precipitated from a precursor solution that also contained an Fe salt. Using hemin and iron nitrate nonahydrate, two ZIF-8 precursor materials were synthesized and named ZIF-8-hem and ZIF-8-nitr, respectively. The colors of the powders were dark greenish for the ZIF-8-hem and white yellowish for the ZIF-8-nitr according to the used Fe-precursors. With the different precursors, the Fe was introduced into the material in two different coordination geometries. Hemin consists of an Fe (III) ion that is coordinated by a porphyrin ring and a chloride ion, which form a square pyramidal complex. In the iron nitrate nonahydrate, the Fe (III) ion is coordinated by six water or methanol molecules arranged in an octahedron. When incorporated into the ZIF-8 lattice consisting of a sodalite structure formed of 2-methylimidazole linkers and tetrahedrally coordinated Zn^{2+} nodes,[60] the two iron precursors behave differently: The hemin is very likely to get encapsulated in the cavities of the ZIF-8, as it has been reported for iron phthalocyanine or iron phenanthroline precursors. In contrast, the iron coordinated by water and methanol partly replaces the Zn^{2+} nodes of the framework.

The crystal structure of the ZIF-8-based materials was investigated via powder X-ray diffraction (XRD), and the diffraction pattern corresponds well to the reference diffractogram of ZIF-8 (Figure 1b). Likewise, the measured elemental composition was measured in combustion elemental analysis, and both precursors match well the predicted composition from calculations (Table S1, Supporting Information). SEM images (Figure 1c; Figure S1a,b, Supporting Information) reveal that the ZIF-8-hem

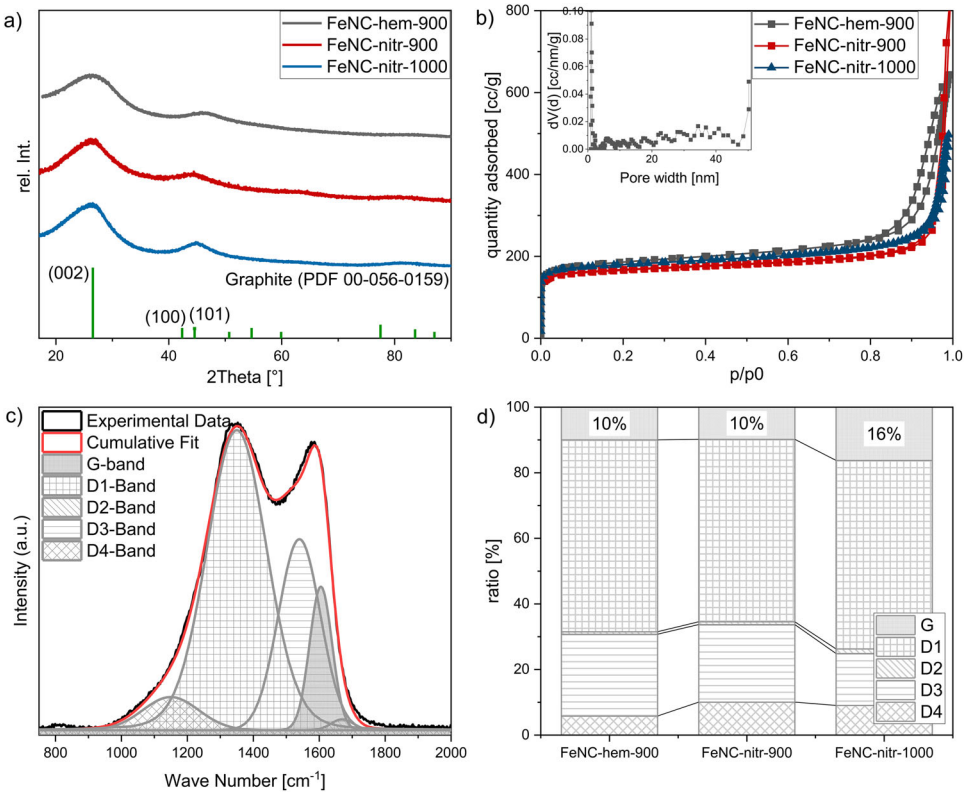

Figure 2. Characterization of the FeNCs in (a) XRD, (b) N_2 physisorption, and (c,d) Raman spectrometry. The Raman spectra of FeNC-nitr-900 and FeNC-nitr-1000 are shown in Figure S6 (Supporting Information).

sample consists of nanoparticles strongly agglomerated with a size of 35 ± 15 nm. In contrast, the ZIF-8-nitr particles show the typical shape of ZIF-8 crystallites, namely rhombic dodecahedrons (Figure 1d; Figure S1c,d, Supporting Information), with a size of 80 ± 20 nm and little agglomeration.

From the N_2 physisorption isotherm, the multi point Brunauer–Emmet–Teller (BET) surface area was determined to be 1178 $m^2\ g^{-1}$ for the ZIF-8-hem and 1095 $m^2\ g^{-1}$ for the ZIF-8-nitr (Figure S2 and Table S2, Supporting Information). The observed pore structure of both ZIF-8 materials mainly consists of micropores <2 nm, which is in good agreement with the ZIF-8 crystal lattice in which the interspace diameter is 1.16 nm. The isotherm of the ZIF-8-hem also shows a small hysteresis at high relative pressures, indicating the presence of larger pores corresponding to the interspace of the agglomerated MOF particles. In the N_2 physisorption isotherm of the ZIF-8-nitr, the hysteresis is much less pronounced.

The Fe and Zn content of the ZIF-8 materials was determined using inductively coupled plasma optical emission spectroscopy (ICP-OES) and found to be 0.2 wt.% Fe and 20.3 wt.% Zn for the ZIF-8-hem (Table S3, Supporting Information). For the ZIF-8-nitr, the Fe content was detemined to account for 0.6 wt.% and the Zn content for 27 wt.%, which is close to the expected stochiometric Zn content of ZIF-8 (= $Zn(C_4N_2H_5)_2$).

In a second step, the ZIF-8 materials are pyrolyzed at 900 °C in inert atmosphere. The ZIF-8-hem yields the FeNC-hem-900 and the ZIF-8-nitr yields the FeNC-nitr-900 samples after pyrolysis. Both products are carbon materials that show the broad (002) and (101) reflections of a partly graphitic but mostly amorphous carbon material in XRD (**Figure 2a**). The SEM images reveal the morphology of the FeNC-hem-900 (Figure S3, Supporting Information) and FeNC-nitr-900 (Figure S4, Supporting Information). After pyrolysis, the FeNC-hem-900 particles are shrunk compared to the ZIF-8-hem particles before pyrolysis (Figure 1c), but they still show the same shape and agglomerated state. The FeNC-nitr-900 particles also show shrinking and the typical rhombic dodecahedral shape of the ZIF-8-nitr precursor particles.

The comparison of the N_2 physisorption isotherms and BET surface area shows that the BET surface area and micropore volume decrease significantly during the pyrolysis of the ZIF-8 precursors to FeNC materials. The BET surface area of the FeNC-hem-900 accounts for 655 $m^2\ g^{-1}$ and the FeNC-nitr-900 for 653 $m^2\ g^{-1}$, so that the two samples are comparable in this aspect (Figure 2b; Figure S5, Supporting Information, for more detail; **Table 1**). Also, for both FeNC materials, the ratio of micropore volume to total volume is much smaller than for the ZIF-8 materials. For both materials, macropores which are the particle interspace contribute to the porosity. For the FeNC-hem-900, there is again a hysteresis observed which indicates the presence of some larger mesopores and smaller particle interspaces. This matches the morphology of the FeNC-hem-900 observed in SEM, where the small interspaces between agglomerated particles are visible.

The analysis of the Raman spectra gives insight into the degree of ordering of the carbon phase of the FeNCs through fitting the measured spectra with a five-band model including the G-, D1,

Table 1. Surface area, pore volume, and average pore size of the FeNCs. Calculations are based on the Brunauer–Emmet–Teller (BET) and the density functional theory (DFT) model.

Sample	BET surface area [$m^2 g^{-1}$]	Cumulative pore volume from DFT [$cm^3 g^{-1}$]	DFT fit performed for pores < ... [nm]	Micropore volume from DFT (diameter < 2 nm) [$cm^3 g^{-1}$]
FeNC-hem-900	655	0.63	50.2	0.23
FeNC-nitr-900	653	0.38	46.9	0.22
FeNC-nitr-1000	696	0.44	50.2	0.24

D2, D3, and D4 bands at 1605, 1365, 1670, 1535, and 1160 cm^{-1} respectively. The fittings show that the contribution of G- and D1-band are very similar for the FeNC-hem-900 and the FeNC-nitr-900 (Figure 2c,d; Figure S6, Supporting Information) and that the samples are very similar in terms of their microstructure.

Elemental analysis indicates a N-content of 14 and 12 wt.% for the FeNC-hem-900 and the FeNC-nitr-900, respectively (**Table 2**). The Zn content of the materials decreases during pyrolysis due to the partial evaporation of zinc (boiling temperature of Zn: 908.5 °C).[61,62] FeNC-hem-900 contains 0.7 wt.% Fe and 11.7 wt.% Zn and FeNC-nitr-900 contains 1.2 wt.% Fe and 6.1 wt.% Zn (Table 2). Crystalline Fe or Zn phases cannot be clearly observed in the powder XRD pattern (Figure 2a). The presence of larger iron and zinc nanoparticles can be excluded, but smaller Fe and Zn metallic or oxide species might still occur. Consequently, the nature of the Fe and Zn entities must be confirmed by further characterization such as HAADF-STEM and XAS. HAADF-STEM images clearly confirm the presence of single atom Fe and Zn sites (**Figure 3**a,b; Figure S7, Supporting Information). Also, some dual atom sites ($FeFeN_x$, $ZnZnN_x$, and $ZnFeN_x$) and clusters are possibly present (Figure S7, Supporting Information). However, their analysis is complicated by the 3D structure, and XAS is required to finally confirm the nature of the metal species.

Analysis of line profiles shows that the atomic diameters of the single atoms are between 280 and 310 pm, which is slightly larger, but corresponds well to the diameters of Zn (270 pm) and Fe (280 pm) (Figures S8 and S9, Supporting Information).[63] From the HR-TEM/EDX mappings, it becomes clear that the density of isolated Fe sites is much lower than the density of Zn sites which is in good agreement with the Fe- and Zn-content from ICP-OES as mentioned above (Figure 3; Figure S10, Supporting Information; Table 2). All in all, the FeNC-hem-900 and the FeNC-nitr-900 are comparable in terms of surface area, degree of graphitization and the absence of larger metallic crystalline domains. The main differences are found in the Fe- and Zn content and the particle size and porosity.

The ZIF-8-nitr was additionally pyrolyzed at 1000 °C in N_2 atmosphere, yielding the sample FeNC-nitr-1000. The product is again a carbonaceous material with amorphous and graphitic domains, resulting in broad reflexes in the powder XRD pattern. Compared to the samples pyrolyzed at 900 °C, the reflexes of the FeNC-nitr-1000 are less broad and more intense, indicating a higher degree of graphitization which is expected for higher temperatures. From the Raman spectra, the contribution of the G-band was determined to be higher than for the FeNCs calcined at 900 °C, confirming the higher degree of graphitization (Figure S6, Supporting Information; Figure 2).

The BET surface area is 692 $m^2 g^{-1}$ and larger than the surface area of the other two samples (Figure 2b, Table 1). The FeNC-nitr-1000 micropores and macropores contribute to the porosity as observed in the N_2-physisorption isotherm. The SEM images show that the FeNC-nitr-1000 has the same particle shape as its precursor (Figure S11, Supporting Information). The nitrogen content is decreased at higher pyrolysis temperature so that the FeNC-nitr-1000 contains only 6 wt.% nitrogen. The zinc is almost completely removed from the material so that only 0.6 wt.% Zn remains while the Fe content is 1.5 wt.%. Again, no larger crystalline phases are observed in powder XRD. HAADF-STEM images show that the Fe and Zn are present in the form of isolated single atom sites as shown in Figure S12 (Supporting Information). The detailed structure of the Fe and Zn species is elucidated by X-ray absorption spectroscopy (XAS).

2.1. Structural Investigation of the Metal Sites

To analyze the short-range atomic order of the FeNC-hem-900, FeNC-nitr-900, and FeNC-nitr-1000, we performed X-ray absorption near edge structure (XANES), and extended X-ray absorption fine structure (EXAFS) analysis at Fe and Zn K-edges, respectively. As shown in **Figure 4**, the Fe and Zn XANES spectra of the FeNC materials and the corresponding reference compounds were investigated. The average oxidation state (AOS) of Fe can be estimated via the K-edge shift from XANES spectra. The main edge in XANES spectra shifts toward higher energy

Table 2. Information on the elemental composition of the FeNCs was determined using elemental analysis and inductively coupled plasma optical emission spectroscopy (ICP-OES).

	Elemental analysis				ICP-OES	
Sample	C [wt.%]	H [wt.%]	N [wt.%]	Rest [wt.%]	Zn [wt.%]	Fe [wt.%]
FeNC-hem-900	64.5	1.9	14.2	19.3	9.8	0.7
FeNC-nitr-900	62.2	2.2	12.5	23.1	6.1	1.2
FeNC-nitr-1000	77.6	1.9	5.8	14.7	0.6	1.5

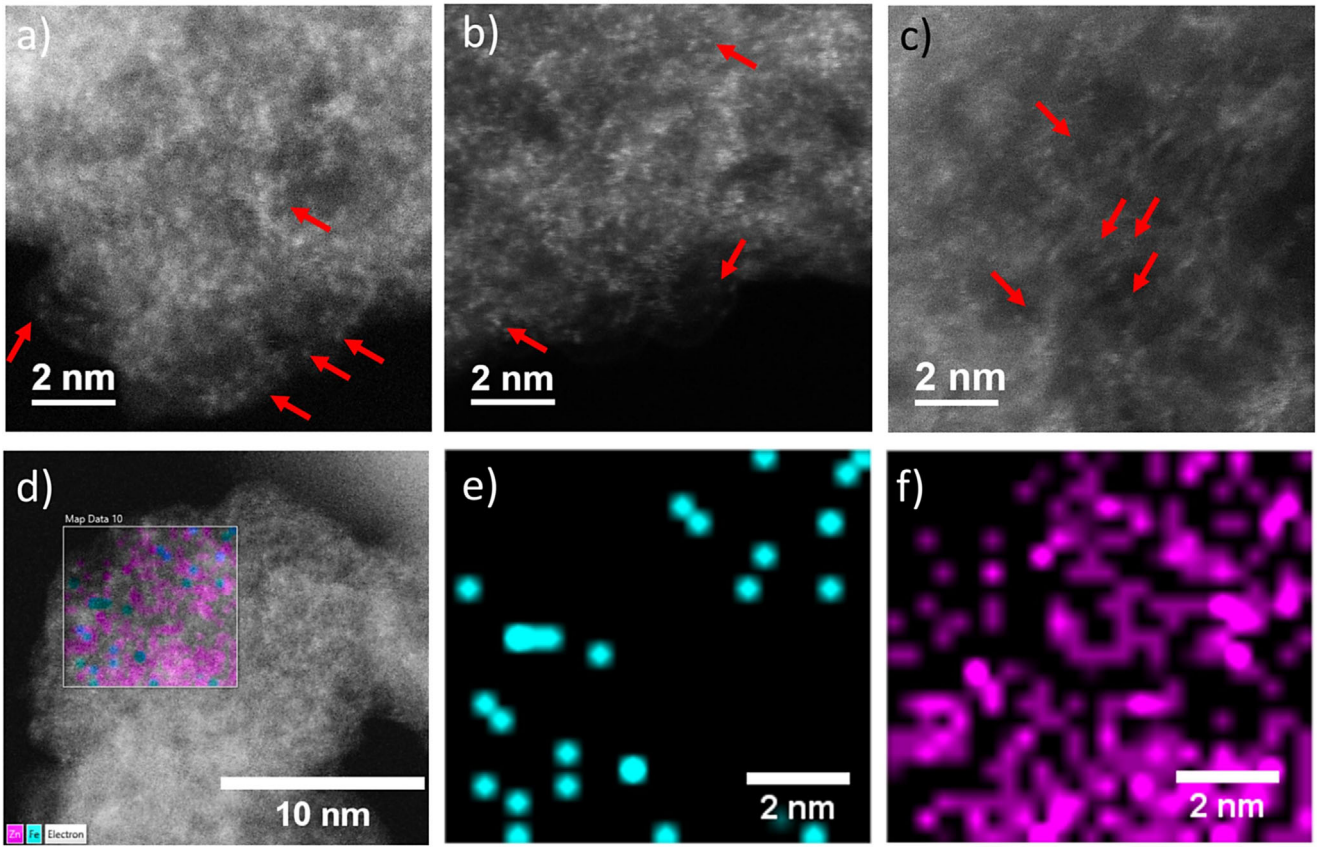

Figure 3. High angle annular dark field scanning electron microscopy (HAADF-STEM) characterization reveals the presence of single atom sites in the FeNC-hem-900 (a), FeNC-nitr-900 (b), and FeNC-nitr-1000 (c). HAADF-STEM energy dispersive X-ray spectroscopy mappings (d) of the FeNC-hem-900 show the presence of isolated Fe (e) and Zn (f) atom sites.

nearly in proportion to the increased oxidation state of iron. On the other hand, the pre-edge position also shifts toward higher energy with increasing oxidation state.[64] For a correct and accurate estimation of the AOS, crystallographic information about the Fe sample is crucial, especially in phases where Fe^{3+} and Fe^{2+} are localized in different site geometries.

The accuracy of the mentioned method is influenced by the local coordination of iron and the crystal structure of the measured material. Deep insight into this factor is necessary for the correct assignment of oxidation states from XANES spectra, and comparisons should be done with reference samples having a similar structure in the pre-edge and edge region.[65] The AOS of the Fe center in FeNC-hem-900 and FeNC-nitr-900, and FeNC-nitr-1000 were estimated from the linear dependence of the Fe main K-edge position at the energy corresponding to a $\mu(E)$-value of 0.5 of the normalized XANES spectra (Figure 4b).[66]

The calibration curve showed the Fe AOS of 2.52, 2.66, and 2.27 for FeNC-hem-900, FeNC-nitr-900, and FeNC-nitr-1000, respectively (Figure 4b). Previous XAS studies on Fe single-atom catalysts embedded in nitrogen-doped carbon structures showed that the AOS of the Fe center in the SACs mixture was higher than zero, which is in line with our results.[67] The pre-edge feature's centroid position and integrated intensity are crucial for determining Fe oxidation state and coordination number.[64]

There is a 1.4 ± 0.1 eV separation between the average pre-edge centroid positions of Fe^{2+} and Fe^{3+}, which allows the pre-edge feature position to measure the average Fe-redox state.[55] The comparison of the pre-edge feature's centroid position in the Fe K-edge XANES spectra of FeNC-hem-900, FeNC-nitr-900, FeNC-nitr-1000, hemin compound, and Fe_2O_3 (Figure 4c) suggests that the AOS of Fe in FeNC-hem-900, FeNC-nitr-900, and FeNC-nitr-1000 are closely aligned with that of the hemin compound, rather than Fe_2O_3 or FeOOH. This observation indicates a similarity in the electronic structure and local environment of the Fe atoms in FeNC-hem-900, FeNC-nitr-900, FeNC-nitr-1000, and the hemin compound.

The formation of Fe—N bonds in FeNC-hem-900, FeNC-nitr-900, and FeNC-nitr-1000 is confirmed by the Fourier transform (FT) k^3-weighted EXAFS in **Figure 5**. Comparing Fourier-transform EXAFS (FT-EXAFS) spectra of Fe K-edge of the samples to the spectra of hemin (Figure 5I,j) revealed dominant coordination shells at ≈1.55 Å corresponding to the Fe—N bond.[67] In the more extended atomic-order range (between ≈2 and 4 Å), no major features are observed in the Fe K-edge FT-EXAFS for FeNC-nitr-1000. However, in FeNC-hem-900, and FeNC-nitr-900, a minor intensity appears between ≈ 2.5 and 3 Å (also visible as a weak intensity in the wavelet-transform (WT)-EXAFS shown in Figure 5d,l), which can be attributed to additional carbon, nitrogen or oxygen atoms in the second or higher coordination

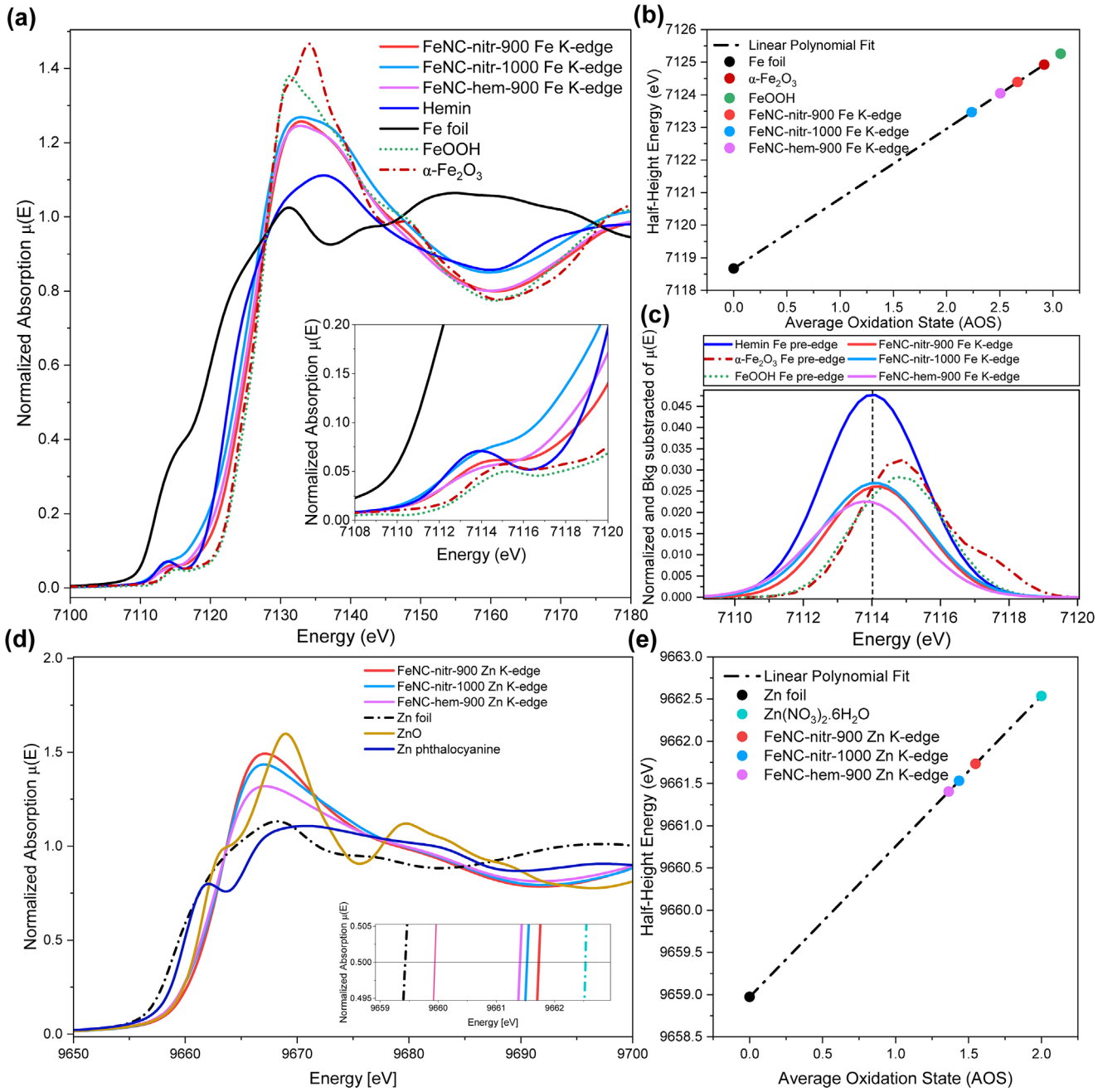

Figure 4. a) Fe K-edge X-ray absorption near edge structure (XANES) spectra of FeNC-hem-900, FeNC-nitr-900, FeNC-nitr-1000, and reference oxides and metallic Fe foil used for energy calibration. b) Linear regression of Fe K-edge energies of FeNC-hem-900, FeNC-nitr-900, FeNC-nitr-1000 and references at 0.5 normalized intensity of XANES spectra. The references are used as a calibration curve for average oxidation state (AOS) calculations. c) The comparison of the pre-edge feature's centroid position in the Fe K-edge XANES spectra of FeNC-hem-900, FeNC-nitr-900, FeNC-nitr-1000, hemin compound, FeOOH, and Fe_2O_3. d) Zn k-edge XANES spectra of FeNC-hem-900, FeNC-nitr-900, FeNC-nitr-1000, and reference for energy calibration. e) Linear regression of Zn K-edge energies of FeNC-hem-900, FeNC-nitr-900, FeNC-nitr-1000, and references at 0.5 normalized intensity of XANES spectra. The references are used as a calibration curve for AOS calculations. Etended X-ray absorption fine structure (EXAFS) analysis can be found in Figure 5 and Figure S13 (Supporting Information).

shells. However, this can also be related to the presence of minor metallic and oxide phases (Figure 5e,f) in FeNC-hem-900 and FeNC-nitr-900. In order to remove iron species other than single atom sites, acid leaching is an established method.[68] During acid leaching the risk of demetallation of the metal centers however prevails, so that we decided not to leach our catalyst materials, which show only negligible oxidic signatures.

The Zn XANES spectra of the FeNC-hem-900, FeNC-nitr-900, FeNC-nitr-1000, and the Zn based reference compound are shown in Figure 4d. The AOS of the Zn center in FeNC-hem-900,

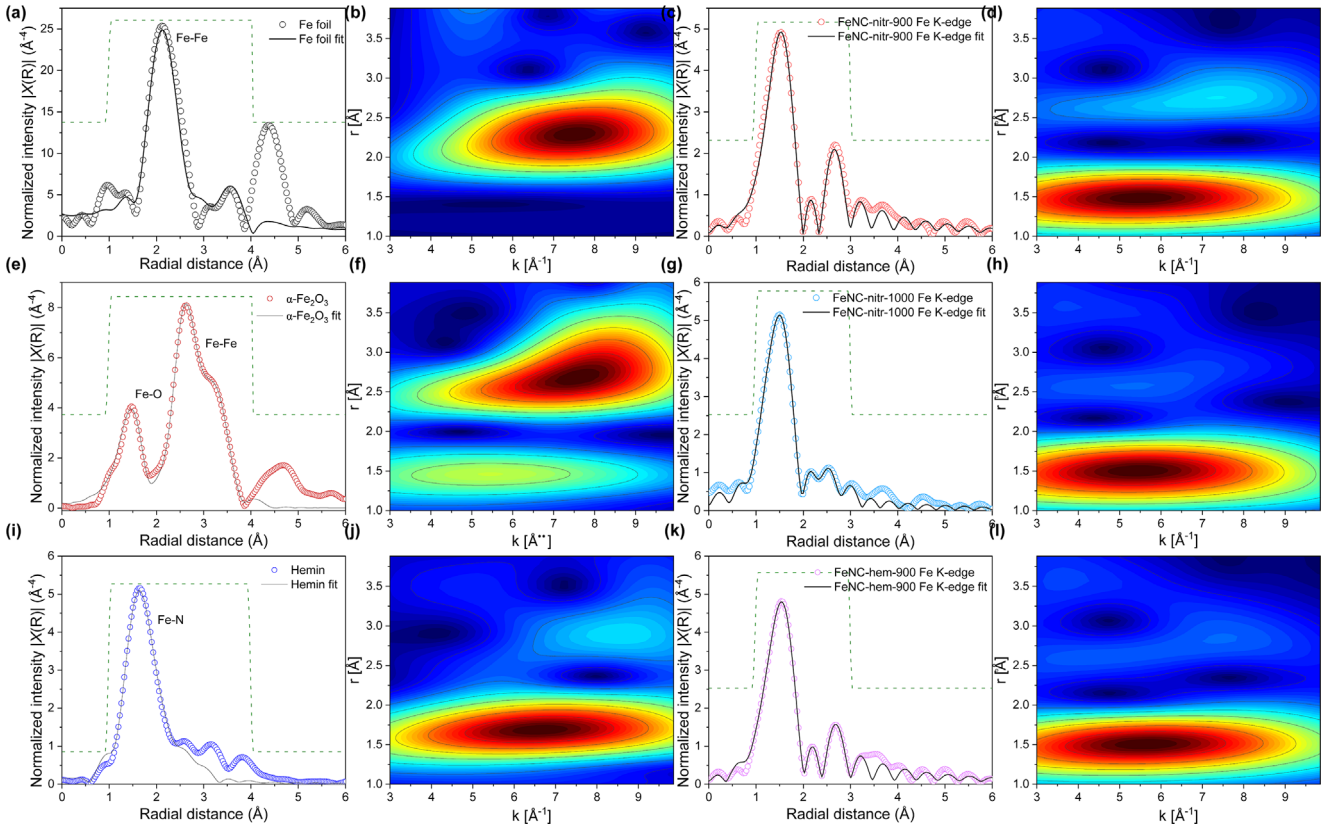

Figure 5. a–l) Comparison of the Fourier-transform Fe K-edge EXAFS spectra and their corresponding Wavelet-transform (WT) ($\eta = 5$ and $\sigma = 2$) of FeNC-hem-900, FeNC-nitr-900, FeNC-nitr-1000, along with reference materials (Fe metallic foil, α-Fe_2O_3, and hemin). The fitting parameters are presented in Tables S4–S15 (Supporting Information).

FeNC-nitr-900, and FeNC-nitr-1000 were estimated from the linear dependence of the Zn main K-edge position at the energy corresponding to a μ(E)-value of 0.5 of the normalized XANES spectra (Figure 4d,e). The calibration curve showed the Zn AOS of 1.37, 1.54, and 1.43 for FeNC-hem-900, FeNC-nitr-900, and FeNC-nitr-1000, respectively (Figure 4e). The AOS below indicates the presence of some metallic zinc phase which is formed during the pyrolysis of the precursor. Comparing Fourier-transform and WT-EXAFS spectra of Zn K-edge in FeNC-hem-900, FeNC-nitr-900, and FeNC-nitr-1000 revealed the main contribution of Zn-N/O around ≈1.55 Å, which points to the presence of Zn single atom sites (Figure S13, fitting parameters in Tables S4–S15, Supporting Information).

3. Electrochemical Performance in eNRR

3.1. The Electrochemical Setup Must Meet the Criteria for Reliable eNRR Measurements

All three FeNC materials, i.e. FeNC-hem-900, FeNC-nitr-900, FeNC-nitr-1000, were tested for nitrogen reduction activity. Special attention was paid to the setup in order to ensure that contamination cannot occur. For the electrochemical tests, all measurements were conducted in an H-cell (2 × 50 mL) in which the two compartments were separated by a proton conducting membrane. The catalysts were coated on carbon paper at 1 mg cm^{-2} and these working electrodes were fixed in the H-cell using a holder with a glassy carbon electrical contact. Pristine carbon paper and an Ag/AgCl (3 M) electrode were used as counter and reference electrode respectively. All gases were used at high purity (99.999%) and were additionally bubbled through alkaline (1 M NaOH) and acidic solution (0.5 M H_2SO_4) before entering the cell. Ammonium was quantified with the indophenol blue method (limit of detection (LOD) = 0.215 μmol L^{-1}) optimized by Biswas et al.[24] The concentrations of nitrite and nitrate were determined using the Griess method[69] (LOD = 0.133 μmol L^{-1}) as shown in Figure S14 (Supporting Information). The NH_3 and NO_x content of the gases after passing the scrubbing system were tested by bubbling through 0.1 M HCl solution for 2 h at 100 mL min^{-1}. The respective concentrations were zero for both ammonia and NO_x (Figure S15, Supporting Information). Hence, the scrubbed gases can be considered suitable for eNRR tests.

Before performance tests, the electrochemical setup was examined for possible sources of contamination. The cell, including the phosphate buffer electrolyte (pH 7.4), the Nafion membrane, the gas connectors, and the three electrodes, did not contain or release any ammonium nor nitrous oxides over the course of several hours, at minimum. The gas outlet of the cell is connected to an acidic trap in which all ammonia potentially outgassed from the cathodic compartment is captured. The initial concentration of NO_x in the H-cell must be zero in order to exclude its

reduction as an ammonia source. Also, the catalyst itself must not release any ammonia nor nitrous oxide species. In order to quantify the contamination from these sources, a catalyst-coated working electrode was kept at OCP in a complete setup for 2 h, the typical duration of a measurement. This was first conducted in Ar- and subsequently in N_2-saturated electrolyte without further pre-conditioning of the WE, while the ammonia and NO_x concentration were monitored. In Ar-saturated electrolyte, the ammonia release during OCP is 0.07 µmol h^{-1} $mg_{cat}{}^{-1}$ and the NO_x release is 0.19 µmol h^{-1} $mg_{cat}{}^{-1}$. However, during the following 2 h of OCP in N_2-saturated electrolyte, neither ammonia nor NO_x were released anymore (Figure S16, Supporting Information).

Three key effects can be observed here: In the first place, it is important to conduct a preconditioning, as there is ammonia and NO_x released in the first 2 h. Second, it becomes clear that during the first 2 h, the contaminant release originates from the setup, as the gas feed was shown to be clean already. Third, during the second 2 h, no contaminants are released, showing that during the second 2 h, the setup neither releases NO_x nor ammonia anymore.

Consequently, it needs to be considered that ammonia and nitrous oxides are present/adsorbed on the as-prepared working electrode. These species desorb in the electrolyte and may falsify the actual ammonia yields in performance measurements. To exclude this effect, a conditioning is mandatory, and a blank must be measured before the performance tests for all performance measurements. In this study, these precautions were taken so that the setup and protocol correspond to the protocol demanded for reliable eNRR results in the literature.[20,70]

3.2. eNRR Performance Tests Using the FeNC Catalysts

A preconditioned FeNC-hem-900 working electrode was measured in linear sweep voltammetry (LSV) in Ar- and N_2-saturated electrolyte (Figure S17, Supporting Information). Under N_2 and Ar atmosphere, the current density under N_2 is slightly increased, but not to the extent that is shown for FeNCs catalyst in literature under the same conditions.[34] However, during chronoamperometry (CA) at the three potentials with highest reported activities, the ammonia yields are below 0.1 µg h^{-1} $mg_{cat}{}^{-1}$ (**Figure 6a**). This is at least one order of magnitude less than the ammonia yield rates reported for iron single site catalysts in eNRR.[33–36,71] Only for the CA at −0.5 V versus RHE, the concentrations were above the limit of detection (LOD).

The FeNC-hem-900, FeNC-nitr-900, and FeNC-nitr-1000 were tested in chronoamperometry at several potentials first under Ar and then under N_2 atmosphere, to ensure the detection of any eNRR activity in the potential range from 0.1 V versus RHE to −0.5 V versus RHE. The working electrode was pre-conditioned and measured in CA for 1 h at 0.1, 0.0, −0.1, −0.2, −0.3, −0.4, and −0.5 V versus RHE, respectively, and the overall ammonia production during these 7 h was determined for both, the experiment under Ar and under N_2 atmosphere (Figure 6b; Figure S18, Supporting Information). For the FeNC-hem-900, the overall ammonia release was 0.17 µg h^{-1} $mg_{cat}{}^{-1}$ in Ar-saturated electrolyte and 0.12 µg h^{-1} $mg_{cat}{}^{-1}$ in N_2-saturated electrolyte. The observation that more ammonia is released under Ar than N_2 points toward NH_3 production from catalyst decomposition rather than from N_2 reduction. Likewise, the FeNC-nitr-900 and FeNC-nitr-1000 were tested, and the overall ammonia yields were shown to be higher under Ar than under N_2 (Figure 6b). We rationalize the "Ar > N_2" baseline observed after pre-conditioning by noting that trace NH_3 detected under Ar arises from labile and reducible nitrogen already present within the porous FeNC materials (e.g., adsorbed NOx/$NO_2{}^-$, edge-pyrrolic/pyridinic groups, or residual precursor fragments) that can be hydrogenated under cathodic bias. This behavior accords with contamination-control guidance and NOx-interference reports.[18,20,53,72] Quantitatively, the amount released (≈1 nmol N during 7 h chronoamperometry at reductive potentials) is <0.1% of the film's nitrogen inventory and therefore does not perturb the Fe—N_4 framework. Consistently, Fe K-edge EXAFS/XRD/HAADF-STEM show atomically dispersed Fe with no Fe—Fe scattering or Fe/FeO_x reflections before/after tests,[35,58] and the catalysts retain high NO_3RR activity (vide infra). Thus, the "Ar > N_2" outcome is diagnostic of catalyst-intrinsic N release rather than N_2 reduction, reinforcing our conclusion that the present FeNC materials are inactive for eNRR under clean, neutral aqueous conditions while being highly selective for $NO_3{}^- \rightarrow NH_3$. These findings contradict previous literature reports that claimed FeNCs materias active for eNRR (Table S16, Supporting Information). To summarize, our study demonstrates that MOF-derived FeNCs materials turn out to be another class of catalysts that, ultimately, exhibit no activity toward the eNRR in aqueous electrolyte at last.

To this conclusion, the objection might be raised that the oxidic iron species present in the FeNC-hem-900 and FeNC-nitr-900 might quench the eNRR activity of the iron single atomic sites. However, we note that large apparent eNRR activities on Fe—N—C frequently coincide with incomplete exclusion of Fe nanoparticles/oxides or NO_x contamination.[18,20,34–36,72,73] By contrast, our XRD, aberration-corrected HAADF-STEM/EDX, and Fe K-edge XAS/EXAFS results collectively evidence atomically dispersed Fe—N_x centers with no diffraction-visible Fe/Fe_xO_y phases; only a minor Fe—O contribution is discernible in the EXAFS fits. The evidence supports that these catalysts are dominated by Fe—N_x single sites and that our contamination-exclusion protocol, rather than the presence/absence of NPs, governs the observed lack of eNRR. We also note that the use of nitrate salts as precursors may introduce NO_x species into the catalyst material, which can cause or enhance the overestimation of the ammonia yield rate. Upon heating to temperatures >140 and >650 °C, $NO_3{}^-$ decomposes to NO_2, NO, and O_2 gases, which can strongly adsorb to the surface after pyrolysis. In our synthesis protocol, the temperature is kept at the targeted pyrolysis temperature for 3 h, which is much longer than reported in other studies on ZIF-8 based FeNCs. A conditioning with subsequent electrolyte exchange also prevents the contribution of adsorbed NO_2. In conclusion, under clean contamination-free conditions FeNC materials do not reduce N_2 to NH_3 in neutral aqueous media, whereas they catalyze the reduction of $NO_3{}^- \rightarrow NH_3$ with high selectivity.[20,58,72]

In the following, a few more aspects of reliable eNRR measurements shall be given. In order to demonstrate the impact of an electrochemical preconditioning and the order of gases, further tests were performed. The FeNC-hem-900 was measured in CA at −0.4 V versus RHE for 2 h each in Ar-saturated, N_2-saturated,

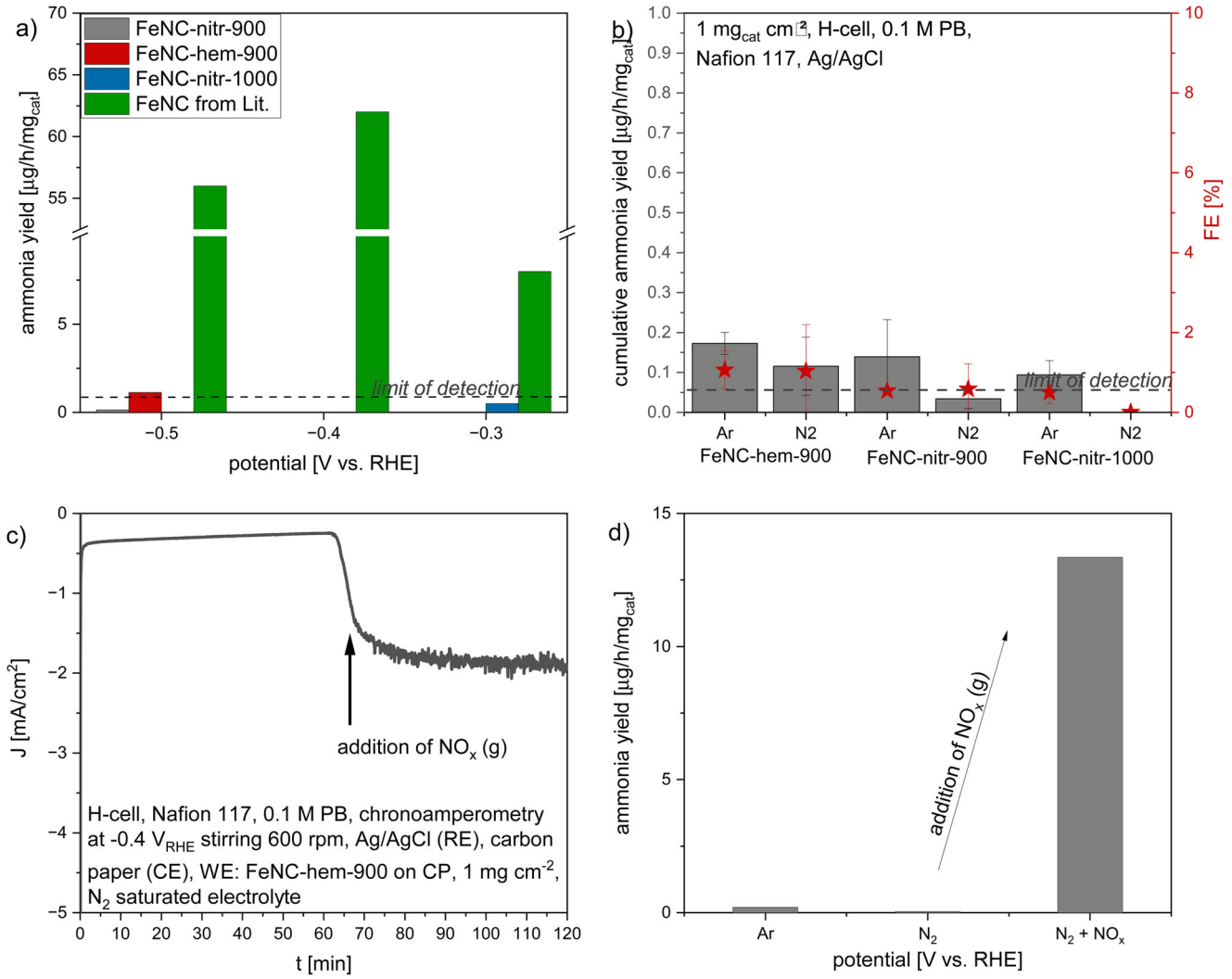

Figure 6. Ammonia yield rates from electrochemical nitrogen reduction reaction (eNRR) performance of the FeNCs measured at three potentials in chronoamperometry (CA) for 2 h each (a). For context, a previously reported study is shown.[34] Cumulative ammonia production rates (b) that were determined from 7 h CA at seven potentials (0.1, 0.0, −0.1 … −0.5 V versus RHE, 1 h hold at every potential) hardly exceed the limit of detection. Error bars signify the mean of n = 3 samples ± standard deviation. (c) CA trace at −0.4 V versus RHE under N_2; a brief addition of a NO/NO_2 (NO_x) trace stream into the gas feed is indicated. (d) Corresponding NH_3 production rate during CA extracted from (c).

and again in Ar-saturated electrolyte. The same was done in the order N_2—Ar—N_2 (Figure S19, Supporting Information). In both cases, no conditioning was used to test ammonia production and its reproducibility when no pre-treatment is applied. The ammonia yield rate was observed to be highest during the first CA and decreased to zero during the following measurements. This was observed for both orders of Ar and N_2. Consequently, the ammonia yield rate of the first CA could not be reproduced in the third CA, regardless of which gas the electrolyte was saturated with. The first ammonia release of an unconditioned electrode cannot be attributed to genuine nitrogen reduction. Especially for nitrogen-containing catalysts, a conditioning and subsequent electrolyte exchange is necessary to ensure reliable results for the eNRR performance. Also, the yields in N_2-saturated electrolyte are not generally higher than in Ar-saturated electrolyte as could be expected for ammonia production from N_2 reduction. For reliable results, the blank measurement under Ar must absolutely be measured before the performance measurement under N_2 atmosphere. It is also mandatory to state the order of the measurements in eNRR reports. In this work, blank measurements were run before the performance measurements in all cases.

One more reason for false positive eNRR results is the presence and reduction of NO_x, NO_2^-, and NO_3^- in the electrolyte. In order to demonstrate this possibility, chronoamperometry was run at −0.4 V versus RHE under N_2 atmosphere, and gaseous NO_x (NO and NO_2) was added to the gas feed (for more details see Experimental Section). As clearly shown in Figure 6c,d, the current density and ammonia yield rate increase upon NO_x addition from almost zero to significant levels. Clearly, the FeNC-hem-900 is active for NO_x reduction to ammonia in aqueous media. The performance for nitrite reduction to ammonia was tested for low concentrations of nitrite (Figure S20, Supporting Information)

and found to be active in a potential range from −0.2 V versus RHE to −0.4 V versus RHE at a nitrite concentration of 30 µM. This overlaps with the potential range where NRR is often tested.

Given this, even small amounts of gaseous and ionic NO_x contaminations can cause overestimated ammonia yield rates or the very appearance of ammonia production, where in clean conditions, no ammonia would have been obtained at all.

With our investigations, we strongly reemphasize the need for proper and well-documented protocols for any eNRR experiments in order to ensure correct results and reproducibility. From our experiments, we can point out the following practical aspects that need to be considered in eNRR experiments:

1) Gases must be free of ammonia and NO_x. The gases should have a minimum purity of 99.999% and must be thoroughly scrubbed before being purged through the electrolyte to avoid any accumulation of N-containing impurities.
2) All parts of the electrochemical cell and all devices used for the experiment must be clean. Ideally, a separate lab should be used for the experiment. No nitric acid or other N-containing solvents must be used for cleaning.
3) Before performance measurement, the working electrode should be conditioned, and the electrolyte should be exchanged afterward.
4) The order of blank and performance measurements must be indicated. Conditionings and blanks must be performed prior to the eNRR measurements and reported.
5) No copper parts should be used within the cell, as it is a good catalyst for contaminant NO_x reduction reactions.[74]
6) Samples should be taken from the electrolyte immediately before and after CA.

In this context, false positives must be prevented, but also false negatives should be excluded. If all measures are taken to prevent overestimated ammonia yield rates and the performance turns out low, certain problems can occur so that ammonia, once produced cannot be detected. Consequently, the following points should not be neglected:

1) Ammonia quantification should be performed directly after the electrochemical tests to exclude outgassing of ammonia from the solution over time.
2) The contact of the working electrode holder should not come into contact with the electrolyte. For example, a Pt contact would catalyze the HER, which would lead to underestimations for the eNRR efficiency (Figure S21, Supporting Information).
3) It must be ensured that the membrane does not leak ammonia from the cathodic to the anodic compartment. If, nevertheless, crossover occurs, the counter electrode should have a sufficiently high overpotential for ammonia oxidation as for example, graphite (Figure S22, Supporting Information).
4) In case, samples should be taken from both compartments of the cell and from the acidic trap solution.
5) No chloride ions should be used in the electrolyte. Otherwise, the chloride ions are oxidized at the anode, and the activated chlorine species act as a re-oxidant for possibly formed ammonia. This effect is often used when nitrate is reduced in order to obtain N_2 and not ammonia.[47]

4. Electrochemical Performance in Nitrate Reduction to Ammonia

Finally, the three FeNC materials presented above were also tested for their catalytic activity for electrochemical nitrate reduction. Again, an H-cell with a Nafion 117 membrane was used for the measurements in K_2SO_4 solution (0.1 M) as a close to neutral electrolyte (pH 6) with or without 0.5 M KNO_3 in the electrolyte. Blank measurements were performed before the performance measurements in all cases. The LSV of FeNC-hem-900 (**Figure** 7a) shows the nitrate reduction starting at a potential of −0.41 V versus RHE in the presence of nitrate. In the absence of nitrate, only hydrogen evolution takes place. LSV of FeNC-nitr-900 and FeNC-nitr-1000 show onset-potentials of −0.55 V versus RHE and −0.58 V versus RHE, respectively. This comparison shows that the iron precursor has a great impact on the NO_3-RR activity. The coordination of the iron in the precursor influences the coordination and electronic state of the iron atoms in the catalyst, which in turn enhances the interaction of the iron site with the nitrate. In hemin, the iron is coordinated by a stable porphyrin ligand, which enables a higher degree of control over the coordination environment in the catalyst material than the hexaaquairon from iron nitrate nonahydrate. Small changes in the first and second coordination shell can have a great influence on the electrocatalytic activity.[56,75]

The FeNC-hem-900 and the FeNC-nitr-1000 show the highest ammonia yields, namely 18.6 mg h^{-1} mg_{cat}^{-1} and 19.1 mg h^{-1} mg_{cat}^{-1} at −1.0 V versus RHE (Figure 7b). Compared to the Zn-free FeNC by Wu et al., the ammonia yield rates are on par, but the onset potentials of the MOF-based FeNCs are approximately 150 mV more negative. The FeNCs show good faradaic efficiencies (Figure 7c). The FeNC-nitr-1000 reaches 100% FE at −0.9 V versus RHE. At more negative potentials, the selectivity for nitrate reduction goes down because the HER is more favorable. The FeNC-hem-900 also reaches 100% FE for ammonia at −1.0 V versus RHE. Accordingly, the FeNC-nitr-1000 shows the best ammonia production performance.

The FeNC-nitr-900 only reaches an ammonia yield rate of 6.0 mg h^{-1} mg_{cat}^{-1} at −1.0 V versus RHE, and the FE for ammonia only reaches 65% at −1.0 V versus RHE as a maximum. The FeNC-nitr-900 is also the sample that shows the strongest features for metallic or oxidic iron species compared to the other two samples.

These measurements were all conducted on working electrodes drop cast on carbon paper with a catalyst loading of 0.4 mg cm^{-2} which makes them comparable to the experiments performed by Wu et al. Further iron and zinc single atom catalysts have been reported for the nitrate reduction to ammonia (Table S17, Supporting Information), but a direct comparison of the catalytic performances is difficult, as the experimental conditions are different in each report. By nominal yield rates, the FeNCs presented in this work are on par with most other FeNCs, however, the best yield rates reported for FeNCs and ZnNCs are twice as high as those for the FeNCs of this work. In terms of faradaic efficiency, the FeNCs of this work are only rivalled by the Fe-ppy SAC by Li et al.[57]

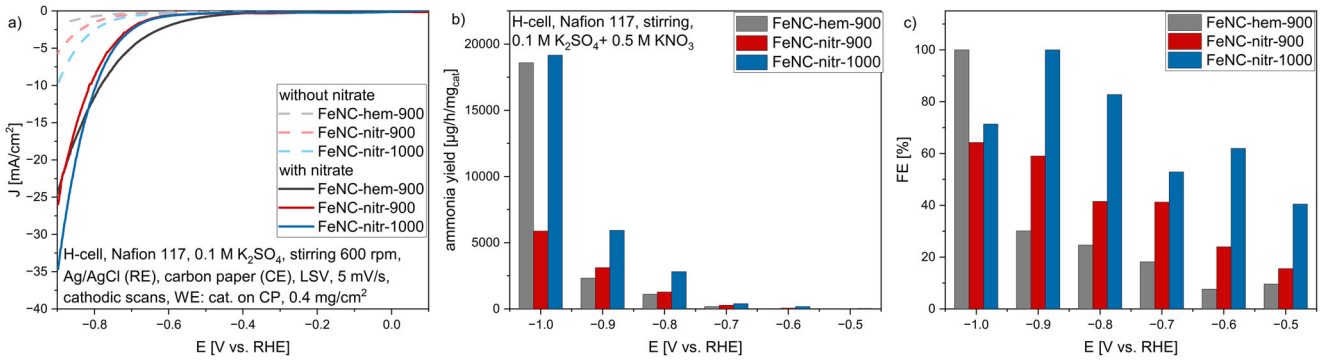

Figure 7. a) Linear sweep voltammogram of the FeNC catalysts with and without KNO_3 in the electrolyte with (b) ammonia yield rates (c) and faradaic efficiencies for ammonia.

In order to elucidate the role of the iron sites in the FeNCs, iron-free NCs were synthesized following the same synthesis protocol but leaving out the iron. The NCs were also characterized (Figure S24 and Table S18, Supporting Information) and measured in NO_3-RR performance experiments and compared to the FeNCs. Figure S25 (Supporting Information) shows that the current densities and ammonia production rates of the NCs are much lower compared to the NCs. This indicates that the iron sites play a crucial role in NO_3-RR activity. The FeNC-nitr-1000 and NC-1000 contain only small amounts of zinc, but the samples pyrolyzed at 900 °C still contain between 6 and 10 wt.% zinc. Comparison of the LSV shows that the presence of iron sites has a greater impact on the current density than the presence of zinc sites. This points to the iron species being the active sites of the FeNC catalyst materials.

The mechanism of the reduction of nitrate to ammonia on iron single atoms is complex, as it involves eight to eleven steps depending on the pH and the calculation.[53,55,58,76] The first steps of the mechanism involve the adsorption of nitrate on the active site, its reduction to adsorbed nitrite, and the further reduction to adsorbed nitric oxide. The next step is the reduction of adsorbed nitric oxide *NO to *NHO, which is also the potential determining step. So far, there is great agreement between different calculations. If subsequently, the *NHO undergoes further reduction via an *NH_2OH intermediate[53,55] or an *N intermediate[58,76] is in debate and depends on the availability of protons, the involvement of the iron coordinating N-atoms and other computational parameters. In both mechanisms, *NO is the intermediate that can also undergo further reduction to N_2 or N_2O.[77] For iron single atomic sites, this combination is calculated to be energetically unfavorable due to the nature of the isolated active sites.[58]

It has further been calculated that the iron single sites favor the potential-determining step as compared to iron nanoparticles.[57] This can be confirmed by our experimental results: The FeNC-nitr-900 shows stronger EXAFS features of metallic or oxidic iron, and at the same time lower faradaic efficiencies and ammonia production performance than the other two samples. The FeNC-nitr-1000, however, shows with 1.5 wt.% the highest iron content. In EXAFS, the features of metallic or oxidic iron are weak, so that most of the iron is present in single atomic sites, which promote the NO_3-RR over the HER.

5. Conclusion

In summary, three different FeNC materials were synthesized successfully via crystallization and pyrolysis of Fe-doped ZIF-8 compounds. Different Fe-precursors and different pyrolysis temperatures yielded the FeNC-hem-900, the FeNC-nitr-900, and the FeNC-nitr-1000, which show different Fe- and Zn-content. None of the three catalysts showed any activity for eNRR in aqueous and ambient conditions after the setup, and the evaluation protocol was ensured to meet all criteria for reliable eNRR measurements: The gases and electrolyte did not contain any ammonia or NO_x contaminations. In this clean setup, only traces of ammonia production were observed, but the small amounts of ammonia that were obtained were attributed to contamination from catalyst decomposition. Although not successful in terms of ammonia production, the process still provides insights into reliable eNRR measurements and into how to prevent false positive and negative results. A possible explanation for the false positives and overestimated ammonia yields reported for eNRR using FeNCs was found in the reduction of NO_x contaminants to ammonia. When NO_x is added to the gas feed, the current density and ammonia yield increase significantly, so that it could be concluded that the FeNCs are active for the NO_x reduction to ammonia. An overview of the FeNCs in comparison with other Fe (and Zn) single atom catalysts is shown in Table S17 (Supporting Information).

The three catalysts were also tested for their activity for electrochemical nitrate reduction to ammonia and proved active. It was found that the ammonia yield rate was related to the Fe-site density on the surface. Consequently, the FeNC with the highest Fe-content of 1.51 wt.% achieved an ammonia yield of 19.1 mg h^{-1} mg_{cat}^{-1} at −1.0 V versus RHE and a maximum FE of 100% at −0.9 V versus RHE, which is comparable to yield rates and FE that have been reported for other Fe(Zn)NCs. The high Fe-content is achieved through a higher pyrolysis temperature of 1000 °C that promotes the evaporation of Zn. It is further observed that the FeNC-hem-900 shows a significantly higher onset potential for the nitrate reduction than the FeNC-nitr-900 and FeNC-nitr-1000. We conclude that the iron precursor has a clear impact on the coordination environment of the iron single atoms and, consequently, also on the electrocatalytic activity. For future experimental studies, it would be important to investigate the influence of the coordination environment of the iron precursor

on the coordination environment in the catalyst material and systematically shed light on the influence on the electrocatalytic activity. DFT investigations and in-situ XAS/FTIR studies would equally be valuable next steps to investigate the influence of the active site and reaction conditions, such as pH, on the NO_3^--to-NH_3 activity.

All in all, FeNCs are suitable catalysts for the nitrate reduction to ammonia. The fact that these catalysts are well known from other electrochemical reactions such as ORR and CO_2RR, opens up a large playground for further optimization of the FeNCs for the NO_3-RR.

6. Experimental Section

Chemicals: All chemicals were used as received unless stated differently. $Fe(NO_3)_3$•9 H_2O (98%+, metal bases) was purchased by Alpha Aesar. $Zn(NO_3)_2$•6 H_2O (≥99% p.a.), ethanol (≥99% p.a.) Potassium nitrate and potassium sulphate (≥99% p.a.) were bought from Carl Roth. Methanol (ACS, Reag. Ph Eur) was purchased VWR. Hemin (≥98%, bioextra), NH_3•H_2O, 2-methylimidazole, carbon paper (Toray, TGP-H-60), Nafion perfluorinated solution, graphite rods (3 mm), NaOH, and H_2SO_4 (98%, for analysis) were bought from Sigma Aldrich. Potassium dihydrogen orthophosphate and dipotassium hydrogen orthophosphate (both analytical reagent grade) as well as hemin (98%, from porcine), were delivered by Fischer Scientific. Hydrochloric acid (99.999% metal basis) was purchased by Thermo Scientific. Deionized water with a resistance of 18 MΩ was provided by a Purelab Flex2 system by Veolia. Ar and N_2 gases were provided in 5.0 purity grade by Sauerstoffwerke Friedrichshafen.

Synthesis of the Fe-Doped ZIF-8: The FeNC materials were synthesized via the pyrolysis of a zinc-imidazole-framework (ZIF-8). The Fe-doped ZIF-8 was synthesized by the following procedure: 2-(methyl)-imidazole (2.89 g) was dissolved in methanol (50 mL, solution A), and $Zn(NO_3)_2$ • 6 H_2O (3.5 g) and hemin (0.5 g) were dissolved in methanol (50 mL, solution B). When clear, solution B was dropped into solution A under stirring. Methanol and NH_3•H_2O solution (30%) were mixed at 3:1 ratio to yield solution C (50 mL), which was quickly dropped into the reaction mixture. After stirring for 1 h, the reaction was heated to 60 °C for 24 h without stirring. The mix was cooled down and the product was obtained by centrifuging and washing four times with methanol (100 mL). Finally, the product was dried at 60 °C in the oven. The obtained sample was noted ZIF-8-hem. With the same procedure, but replacing the hemin by $Fe(NO_3)_3$ • 9 H_2O (124 mg), the sample ZIF-8-nitr was obtained.

Synthesis of the FeNC Materials: The ZIF-8-hem was pyrolyzed at 900 °C to yield the sample FeNC-hem-900. For pyrolysis, 600 mg samples were placed in a ceramic boat in a tube furnace. Under N_2 atmosphere, the sample was first heated to 120 °C with 2 K min^{-1} and then to the target temperature with a ramp of 5 K min^{-1}. The sample was held at the target temperature for 3 h. ZIF-8-nitr was pyrolyzed at 900 °C and 1000 °C producing the samples FeNC-nitr-900 and FeNC-nitr-1000.

Synthesis of the iron-free ZIF-8 and NC materials: An undoped ZIF-8 sample was synthesized following the same procedure as described in Section 6.2 and referred to as ZIF-8-noFe.

The ZIF-8-noFe was pyrolyzed at 900 and 1000 °C as described in Section 6.3 to yield the samples NC-900 and NC-1000, respectively.

Physical Characterization: All samples were characterized in X-ray diffraction, N_2 physisorption, elemental analysis, and scanning electron microscopy. For X-ray diffraction, a Bruker D8 DISCOVER using Copper as X-ray source. N_2 physisorption was measured on a 3P Micro 300 at 77 K. Prior to the physisorption measurements, the samples were degassed at 200 °C for 6 h. Specific surface area and pore size distribution were determined using multi-point BET and DFT method, respectively. Elemental analysis was performed on a Vario EL combustion elemental analysis system. Morphology and particle size were analyzed from micrographs taken on a Hitachi SU8220 scanning electron microscope. Energy dispersive X-ray spectroscopy was performed using a Bruker Flat Quad and X-flash EDX detector. Fe content was investigated from burnt and dissolved samples via inductively coupled plasma optical emission spectroscopy with a Spectroblue EOP TI. The FeNC materials were further characterized in Raman spectroscopy using a Senterra II by Bruker Optics with a Laser of 532 nm wavelength. The measurements were performed with a resolution of 4 cm^{-1} in between 50 and 4200 cm^{-1} at 0.25 mW, and UV/VIS spectrometry was performed on a Cary 50 Conc by Varian. XAS data were collected in transmission and fluorescence modes at the SuperXAS beamline at the Paul Scherrer Institute (PSI). XAS was measured at the Fe K-edge and Zn K-edge for the samples and the corresponding references. The measured k^3-weighted extended X-ray absorption fine structure (EXAFS) spectra $k^3\chi(k)$ were extracted by standard data reduction, absorption edge energy calibration, and background subtraction as implemented in ATHENA. The spectra were reduced into the range $\Delta k \approx 3$–11 $Å^{-1}$, and Fourier transformed to FT$|k^3\chi(k)|$ into the real-space interval $\Delta R \approx 0$–6 Å.

Statistical Analysis: To determine the particle size of the ZIF-8, the length of n = 200 particles was measured in a SEM micrograph using ImageJ. The particle sizes are indicated as Mean ± standard deviation.

The determination of the cumulative ammonia production rates was conducted three times, and the average ± standard deviation is presented in Figure 6.

Working electrode preparation: The catalyst (0.4 mg) was mixed thoroughly with Nafion solution (10 µL, 5 wt.% solution) and Ethanol (100 µL) by ultrasonication using an ultrasonic finger. The ink was then drop cast onto a precut L-shaped carbon paper electrode, so that the ink covered 1 cm^2 of the electrode (Figure S21, Supporting Information). The electrode was dried at 60 °C in a drying oven.

Electrochemical Characterization: All electrochemical measurements were performed using a Gamry reference 600+ potentiostat and an H-cell (2 × 50 mL) in which the two compartments were separated by a Nafion 117 membrane. Prior to use, the membranes were pretreated as recommended.[23] Catalyst coated carbon paper, Ag/AgCl (3 M KCl), and carbon paper were used as the working electrode, reference electrode, and counter electrode, respectively. The employed gases, Ar and N_2, were of 99.999% purity and were each bubbled through an acidic and an alkaline trap solution (1 M H_2SO_4 and 1 M NaOH) before being directed through the solution. Therefore, impingers with glass frits were filled with glass balls to ensure a sufficient removal of any impurities from the gas. The gas outflow from the H-cell was directed through 0.1 M HCl solution to trap outgassing ammonia. Ammonium was always quantified in anodic and cathodic compartment and trap solution.

For eNRR experiments, phosphate buffer (0.1 M) was used as electrolyte. Before a typical performance measurement, the electrolyte was saturated with Ar at 100 sccm. The gas flow was then set to 20 sccm and the stir rate to 600 rpm. A conditioning of 300 cycles at 100 mV s^{-1} in the potential range of the LSV was run. After the conditioning, the electrolyte was exchanged and saturated with Ar again in the same manner. Blank measurements were always run first before the performance measurements in N_2 saturated electrolyte. Samples from the electrolyte were always taken immediately before and after CA. From these, ammonia and NO_x were quantified without dilution.

For the demonstration of NO_x reduction, Conditioning, LSV, and CA in Ar and N_2 atmosphere were measured as described above. A second CA was run under N_2 and after 1 h, NO_x was produced from the reaction of copper and nitric acid as described by Choi et al.[20] and added to the gas feed.

For NO_3-RR experiments, Ar saturated K_2SO_4 solution (0.1 M) was used for conditioning and blank measurements, which were always carried out before performance measurements. For the latter, the cathode compartment was filled with KNO_3 (0.5 M) in K_2SO_4 (0.1 M) solution. Also, for the NO_3-RR measurements, the scrubbing system was used for the 5.0 Ar flow, and the same flow rates for saturation and measurement as for the eNRR experiments.

Ammonia Quantification: Ammonia was quantified via the salicylate method.[24] The sample (1 mL) was mixed with a sodium salicylate and trisodium citrate solution (1 mL, 5 wt.% respectively in 1 M NaOH), NaClO solution (0.5 mL, 0.05 M), and sodium nitroprusside solution (0.1 mL,

1 wt.%). After proper mixing, the mixtures were brought to react for 1 h at room temperature before absorbance was measured in UV/VIS spectrometry. After background subtraction, the absorbance at 650 nm wavelength was used for quantification. A calibration curve was prepared by measuring solutions with known NH_4Cl concentration in 0.1 M phosphate buffer or K_2SO_4 solution, respectively. The NH_4Cl standard solutions were diluted from a 100 µM solutions before each measurement.

NO_x Quantification: The Griess method was employed for the quantification of NO_x species.[69] Therefore, the sample (2 mL) was mixed with H_2SO_4 solution (1 M, 400 µL), VCl_3 solution (2 wt.%, 130 µL), and Griess reagent (100 µL). The latter was mixed 1:1 from a sulphanilamide solution (10 wt.% in 2 M HCl) and an N-(1-naphthyl)-ethylenediamine dihydrochloride (NED) solution (0.02 wt.%). The calibration curve was prepared by measuring standard solutions with known concentrations of KNO_3 in 0.1 M phosphate buffer or K_2SO_4 solution, respectively.

Calculation of Yield Rate and Efficiencies: The ammonia yield rate r_{NH3} indicates the amount of ammonia m_{NH3} produced per time t and mass of catalyst m_{cat}. It is indicated as µg h^{-1} mg_{cat}^{-1}.

$$r_{NH_3} = \frac{m_{NH_3}}{t \cdot m_{cat}} \tag{7}$$

The selectivity of a catalyst is indicated by the faradaic efficiency (*FE*), which indicates the ratio of charge that goes into ammonia production and the overall charge:

$$FE = \frac{z \cdot F \cdot n_{NH_3}}{Q} \times 100\% \tag{8}$$

Whereas z is the number of electrons required for the reduction, F is the Faraday constant, n_{NH3} is the amount of ammonia produced in a certain time, and Q is the charge flow during this time.

Supporting Information

Supporting Information is available from the Wiley Online Library or from the author.

Acknowledgements

Funding was provided by core support of the Albert-Ludwigs-Universität Freiburg, by The Volkswagen Foundation (Momentum – Funding for Recently Tenured Professors, "In-Situ Electrochemical Transmission Electron Microscopy – Understanding Electrocatalysts Dynamics under Electrochemical Conditions at the Nano Scale", grantee A.F.) and the Deutsche Forschungsgemeinschaft (DFG) under German's Excellence Strategy (EXC 2193/1 390951807, Cluster of Excellence "Living, adaptive and energy-autonomous Materials Systems", livMatS, grantee A.F.). High resolution transmission electron microscopy infrastructure was provided by the core facility "Imaging of Material Systems" of the FIT – Freiburg Center for Interactive Materials and Bioinspired Technologies of Albert-Ludwigs-Universität Freiburg. The XAS data were collected at the Swiss Light Source (SLS), SuperXAS beamline (X10DA) at the Paul Scherrer Institute (PSI). S.E.B. and the co-authors gratefully acknowledge the SuperXAS team, especially Dr. Olga Safonova, for their support. The authors thank Diamond Light Source for access and support in the use of the electron Physical Science Imaging Centre (Instrument E02 and proposal number MG 33430) that contributed to the results presented here. ICP-OES was measured at the Chair of Geobotany of the Faculty of Biology II of Albert-Ludwigs-Universität Freiburg.

Open access funding enabled and organized by Projekt DEAL.

Conflict of Interest

The authors declare no conflict of interest.

Author Contributions

A.F. initiated this research, provided funding and resources, and designed, supervised, and coordinated the study. A.F. and C.S. designed the material synthesis and electrochemical experiments. C.S. performed the material synthesis. C.S., P.E., N.O., and S.E.B. performed the material characterization with XRD, EA, ICP, BET, SEM, and TEM, along with the corresponding data analysis. C.S. performed the electrochemical measurements. C.S., S.H., P.E., and N.O. worked on the benchmarking of the electrochemical setup for eNRR and NO_3-RR. S.E.B. performed the XAS measurements and the XANES and EXAFS data analysis. C.A. performed the HAADS-STEM measurements. C.S., S.E.B., and A.F. designed, wrote and edited the manuscript. All authors have read and revised the manuscript and agreed to its content.

Data Availability Statement

The data that support the findings of this study are available from the corresponding author upon reasonable request.

Keywords

electrochemical nitrate reduction, Fe—N—C single-atom catalyst, MOF-based catalysts, nitrogen reduction reaction, reevaluation, sustainable ammonia synthesis, ZIF-8-derived Fe single-atom catalyst

Received: June 9, 2025
Revised: September 21, 2025
Published online:

[1] H. Liu, *Chin. J. Catal.* **2014**, *35*, 1619.
[2] V. Pattabathula, J. Richardson, *Back to Basics* **2016**.
[3] M. H. Hasan, T. M. I. Mahlia, M. Mofijur, I. M. Rizwanul Fattah, F. Handayani, H. C. Ong, A. S. Silitonga, *Energies* **2021**, *14*, 3732.
[4] J. Lim, C. A. Fernández, S. W. Lee, M. C. Hatzell, *ACS Energy Lett.* **2021**, *6*, 3676.
[5] D. R. MacFarlane, P. V. Cherepanov, J. Choi, B. H. R. Suryanto, R. Y. Hodgetts, J. M. Bakker, F. M. Ferrero Vallana, A. N. Simonov, *Joule* **2020**, *4*, 1186.
[6] European Hydrogen Observatory, Clean Hydrogen JU, *The European hydrogen market landscape – November, Clean Hydrogen JU*, Brussels, Belgium, **2024**.
[7] L. Ye, R. Nayak-Luke, R. Bañares-Alcántara, E. Tsang, *Chem* **2017**, *3*, 712.
[8] E. E. Van Tamelen, D. A. Seeley, *J. Am. Chem. Soc.* **1969**, *91*, 5194.
[9] G. Chen, S. Ren, L. Zhang, H. Cheng, Y. Luo, K. Zhu, L. Ding, H. Wang, *Small Methods* **2019**, *3*, 1800337.
[10] T. Wu, W. Fan, Y. Zhang, F. Zhang, *Mater. Today Phys.* **2021**, *16*, 100310.
[11] W. Guo, K. Zhang, Z. Liang, R. Zou, Q. Xu, *Chem. Soc. Rev.* **2019**, *48*, 5658.
[12] In *Multiphase Flow Dynamics 4*, Springer, Berlin Heidelberg, Berlin, Heidelberg, **2011**, p. 209–239.
[13] P. Carro, J. Choi, D. R. MacFarlane, A. N. Simonov, J. M. Doña-Rodríguez, L. M. Azofra, *Catal. Sci. Technol.* **2022**, *12*, 2856.
[14] Y. Ren, C. Yu, X. Tan, H. Huang, Q. Wei, J. Qiu, *Energy Environ. Sci.* **2021**, *14*, 1176.
[15] X. Cui, C. Tang, Q. Zhang, *Adv. Energy Mater.* **2018**, *8*, 1800369.
[16] K. Kim, C.-Y. Yoo, J.-N. Kim, H. C. Yoon, J.-I. Han, *J. Electrochem. Soc.* **2016**, *163*, F1523.
[17] H.-L. Du, T. R. Gengenbach, R. Hodgetts, D. R. MacFarlane, A. N. Simonov, *ACS Sustainable Chem. Eng.* **2019**, *7*, 6839.

[18] S. Z. Andersen, V. Čolić, S. Yang, J. A. Schwalbe, A. C. Nielander, J. M. McEnaney, K. Enemark-Rasmussen, J. G. Baker, A. R. Singh, B. A. Rohr, M. J. Statt, S. J. Blair, S. Mezzavilla, J. Kibsgaard, P. C. K. Vesborg, M. Cargnello, S. F. Bent, T. F. Jaramillo, I. E. L. Stephens, J. K. Nørskov, I. Chorkendorff, *Nature* **2019**, *570*, 504.
[19] J. Choi, H.-L. Du, C. K. Nguyen, B. H. R. Suryanto, A. N. Simonov, D. R. MacFarlane, *ACS Energy Lett.* **2020**, *5*, 2095.
[20] J. Choi, B. H. R. Suryanto, D. Wang, H.-L. Du, R. Y. Hodgetts, F. M. Ferrero Vallana, D. R. MacFarlane, A. N. Simonov, *Nat. Commun.* **2020**, *11*, 5546.
[21] C. Tang, S.-Z. Qiao, *Chem. Soc. Rev.* **2019**, *48*, 3166.
[22] Y. Ren, C. Yu, X. Tan, X. Han, H. Huang, H. Huang, J. Qiu, *Small Methods* **2019**, *3*, 1900474.
[23] F. Hanifpour, A. Sveinbjörnsson, C. P. Canales, E. Skúlason, H. D. Flosadóttir, *Angew Chem Int Ed* **2020**, *59*, 22938.
[24] S. S. Biswas, A. Saha, M. Eswaramoorthy, *ACS Omega* **2022**, *7*, 1874.
[25] C. Tang, S.-Z. Qiao, *Joule* **2019**, *3*, 1573.
[26] Y. Zhao, R. Shi, X. Bian, C. Zhou, Y. Zhao, S. Zhang, F. Wu, G. I. N. Waterhouse, L. Wu, C. Tung, T. Zhang, *Adv. Sci.* **2019**, *6*, 1802109.
[27] X. Cai, F. Yang, L. An, C. Fu, L. Luo, S. Shen, J. Zhang, *ChemSusChem* **2022**, *15*, 202102234.
[28] J. Choi, H.-L. Du, M. Chatti, B. H. R. Suryanto, A. N. Simonov, D. R. MacFarlane, *Nat. Catal.* **2022**, *5*, 382.
[29] B. Izelaar, D. Ripepi, S. Asperti, A. I. Dugulan, R. W. A. Hendrikx, A. J. Böttger, F. M. Mulder, R. Kortlever, *ACS Catal.* **2023**, *13*, 1649.
[30] C. Trncik, F. Detemple, O. Einsle, *Nat. Catal.* **2023**, *6*, 415.
[31] J. S. Anderson, J. Rittle, J. C. Peters, *Nature* **2013**, *501*, 84.
[32] X. F. Li, Q. K. Li, J. Cheng, L. Liu, Q. Yan, Y. Wu, X. H. Zhang, Z. Y. Wang, Q. Qiu, Y. Luo, *J. Am. Chem. Soc.* **2016**, *138*, 8706.
[33] M. Wang, S. Liu, T. Qian, J. Liu, J. Zhou, H. Ji, J. Xiong, J. Zhong, C. Yan, *Nat. Commun.* **2019**, *10*, 341.
[34] F. Lü, S. Zhao, R. Guo, J. He, X. Peng, H. Bao, J. Fu, L. Han, G. Qi, J. Luo, X. Tang, X. Liu, *Nano Energy* **2019**, *61*, 420.
[35] R. Zhang, L. Jiao, W. Yang, G. Wan, H. L. Jiang, *J. Mater. Chem. A* **2019**, *7*, 26371.
[36] F. Xu, L. Zhang, X. Ding, M. Cong, Y. Jin, L. Chen, Y. Gao, *Chem. Commun.* **2019**, *55*, 14111.
[37] L. Zhang, G. Fan, W. Xu, M. Yu, L. Wang, Z. Yan, F. Cheng, *Chem. Commun.* **2020**, *56*, 11957.
[38] A. M. Agour, E. Elkersh, G. E. Khedr, H. G. El-Aqapa, N. K. Allam, *ACS Appl. Nano Mater.* **2023**, *6*, 15980.
[39] C. Gao, S. Mu, R. Yan, F. Chen, T. Ma, S. Cao, S. Li, L. Ma, Y. Wang, C. Cheng, *Small* **2022**, *2105409*, 1.
[40] K. Srinivas, Z. Chen, H. Yu, D. Liu, J. Z. Ou, M. Zhu, Y. Chen, *Electron* **2024**, *2*, 26.
[41] M.-J. Kim, S. Kim, J. E. Park, C.-C. Hwang, S. Lee, S. Y. Kang, D. Jung, Y.-H. Cho, J. Kim, K.-S. Lee, Y.-E. Sung, *Nano Energy* **2020**, *78*, 105395.
[42] M. Wang, L. Wang, Q. Li, D. Wang, L. Yang, Y. Han, Y. Ren, G. Tian, X. Zheng, M. Ji, C. Zhu, L. Peng, G. I. N. Waterhouse, *Small* **2023**, *19*, 2300373.
[43] Y. Liu, Y. Su, X. Quan, X. Fan, S. Chen, H. Yu, H. Zhao, Y. Zhang, J. Zhao, *ACS Catal.* **2018**, *8*, 1186.
[44] F. Wang, J. Mao, *Diamond Relat. Mater.* **2021**, *118*, 108494.
[45] Y. Zeng, C. Priest, G. Wang, G. Wu, *Small Methods* **2020**, *4*, 2000672.
[46] H. Xu, Y. Ma, J. Chen, W. Zhang, J. Yang, *Chem. Soc. Rev.* **2022**, *51*, 2710.
[47] I. Zhu, T. Getting, *Environ. Technol. Rev.* **2012**, *1*, 46.
[48] S. Garcia-Segura, M. Lanzarini-Lopes, K. Hristovski, P. Westerhoff, *Appl. Catal., B* **2018**, *236*, 546.
[49] P. H. Van Langevelde, I. Katsounaros, M. T. M. Koper, *Joule* **2021**, *5*, 290.
[50] J. D. Brender, in *Just Enough Nitrogen* (Eds.: M. A. Sutton, K. E. Mason, A. Bleeker, W. K. Hicks, C. Masso, N. Raghuram, S. Reis, M. Bekunda), Springer International Publishing, Cham, pp. 283.
[51] W. Jung, Y. J. Hwang, *Mater. Chem. Front.* **2021**, *5*, 6803.
[52] J. Gao, N. Shi, Y. Li, B. Jiang, T. Marhaba, W. Zhang, *Environ. Sci. Technol.* **2022**, *56*, 11602.
[53] Y. Wang, M. Shao, *ACS Catal.* **2022**, *12*, 5407.
[54] J.-X. Liu, D. Richards, N. Singh, B. R. Goldsmith, *ACS Catal.* **2019**, *9*, 7052.
[55] X. Cheng, W. Shang, Y. Li, J. Hu, J. Guo, D. Cao, N. Zhang, S. Zhang, S. Song, T. Liu, W. Liu, Y. Shi, *Nano Res.* **2024**, *17*, 6826.
[56] Y. Tan, J. Fu, T. Luo, K. Liu, M. Liu, *J. Am. Chem. Soc.* **2025**, *147*, 4937.
[57] P. Li, Z. Jin, Z. Fang, G. Yu, *Energy Environ. Sci.* **2021**, *14*, 3522.
[58] Z.-Y. Wu, M. Karamad, X. Yong, Q. Huang, D. A. Cullen, P. Zhu, C. Xia, Q. Xiao, M. Shakouri, F.-Y. Chen, J. Y. Kim, Y. Xia, K. Heck, Y. Hu, M. S. Wong, Q. Li, I. Gates, S. Siahrostami, H. Wang, *Nat. Commun.* **2021**, *12*, 2870.
[59] J. Zhao, X. Ren, X. Liu, X. Kuang, H. Wang, C. Zhang, Q. Wei, D. Wu, *Chem. Eng. J.* **2023**, *452*, 139533.
[60] K. S. Park, Z. Ni, A. P. Côté, J. Y. Choi, R. Huang, F. J. Uribe-Romo, H. K. Chae, M. O'Keeffe, O. M. Yaghi, *Proc. Natl. Acad. Sci. U.S.A.* **2006**, *103*, 10186.
[61] A. F. Holleman, E. Und Nils Wiberg, G. Fischer, *Lehrbuch der Anorganischen Chemie*, Walter De Gruyter, Berlin, New York, **2007**.
[62] Z. Song, L. Zhang, K. Doyle-Davis, X. Fu, J. Luo, X. Sun, *Adv. Energy Mater.* **2020**, *10*, 2001561.
[63] J. C. Slater, *J. Chem. Phys.* **1964**, *41*, 3199.
[64] M. Wilke, F. Farges, P.-E. Petit, G. E. Brown, F. Martin, *Am. Mineral.* **2001**, *86*, 714.
[65] J. Zhu, Z. Zeng, W.-X. Li, *J. Phys. Chem. C* **2021**, *125*, 26229.
[66] H. Dau, P. Liebisch, M. Haumann, *Anal. Bioanal. Chem.* **2003**, *376*, 562.
[67] J. Wang, B. Li, Y. Li, X. Fan, F. Zhang, G. Zhang, W. Peng, *Adv. Sci.* **2021**, *8*, 2101824.
[68] Y. Zeng, E. Almatrafi, W. Xia, B. Song, W. Xiong, M. Cheng, Z. Wang, Y. Liang, G. Zeng, C. Zhou, *Coord. Chem. Rev.* **2023**, *475*, 214874.
[69] E. García-Robledo, A. Corzo, S. Papaspyrou, *Mar. Chem.* **2014**, *162*, 30.
[70] H. Liu, N. Guijarro, J. Luo, *J. Energy Chem.* **2021**, *61*, 149.
[71] Y. Wang, X. Cui, J. Zhao, G. Jia, L. Gu, Q. Zhang, L. Meng, Z. Shi, L. Zheng, C. Wang, Z. Zhang, W. Zheng, *ACS Catal.* **2019**, *9*, 336.
[72] L. F. Greenlee, J. N. Renner, S. L. Foster, *ACS Catal.* **2018**, *8*, 7820.
[73] A. M. Agour, E. Elkersh, G. E. Khedr, H. G. El-aqapa, N. K. Allam, *ACS Applied Nanomaterials* **2023**, *6*, 15980.
[74] M. Teng, J. Ye, C. Wan, G. He, H. Chen, *Ind. Eng. Chem. Res.* **2022**, *61*, 14731.
[75] J. Xu, S. Zhang, H. Liu, S. Liu, Y. Yuan, Y. Meng, M. Wang, C. Shen, Q. Peng, J. Chen, X. Wang, L. Song, K. Li, W. Chen, *Angew Chem Int Ed* **2023**, *62*, 202308044.
[76] S. Wang, H. Gao, L. Li, K. S. Hui, D. A. Dinh, S. Wu, S. Kumar, F. Chen, Z. Shao, K. N. Hui, *Nano Energy* **2022**, *100*, 107517.
[77] Y. Wang, C. Wang, M. Li, Y. Yu, B. Zhang, *Chem. Soc. Rev.* **2021**, *50*, 6720.